

Global atmospheric hydrogen chemistry and **long-term** source-sink budget equilibrium simulation with the EMAC v2.55 model

Nic Surawski^{1,2}, Benedikt Steil², Christoph Brühl², Sergey Gromov², Klaus Klingmüller², Anna Martin², Andrea Pozzer^{2,3}, and Jos Lelieveld^{2,3}

¹Centre for Green Technology, University of Technology Sydney, Gadigal Country, Ultimo NSW 2007, Australia

²Atmospheric Chemistry Department, Max Planck Institute for Chemistry, 55128 Mainz, Germany

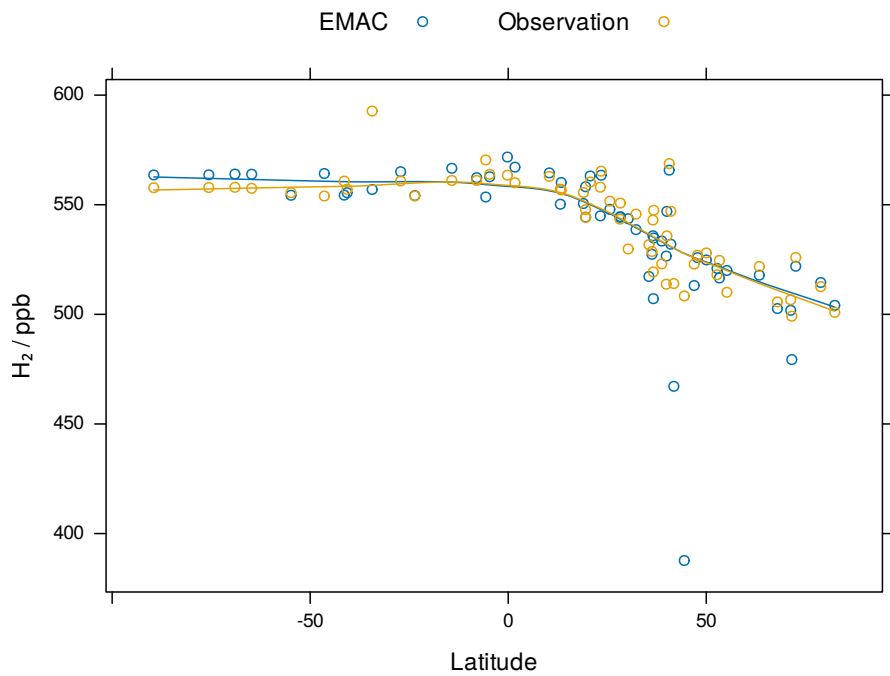
³Climate and Atmosphere Research Center, The Cyprus Institute, Nicosia, Cyprus

Correspondence: Nic Surawski (Nicholas.Surawski@uts.edu.au)

Abstract

In this study, we use an earth system model with detailed atmospheric chemistry (EMAC v2.55.2) to undertake simulations of hydrogen (H_2) atmospheric dynamics. **Long-term Extensive** global equilibrium simulations were performed with a horizontal resolution of 1.9 degrees. The results of this simulation are compared with **long-term** observational data from 56 stations in the

5 National Oceanic and Atmospheric Administration (NOAA) Global Monitoring Laboratory (GML) Carbon Cycle Cooperative Global Air Sampling Network. We introduced H_2 sources and sinks, the latter inclusive of a soil uptake scheme, that accounts for bacterial consumption. The model thus accounts for detailed H_2 and methane (CH_4) flux boundary conditions. Results from the EMAC model are accurate and predict the magnitude, amplitude and interhemispheric seasonality of the annual H_2 cycle at most observational stations. Time series comparison of EMAC and observational data produces Pearson correlation 10 coefficients (r) in excess of 0.9 at eight **stations that experience well-mixed unpolluted air masses** **remote stations located in polar regions and on high mid-latitude islands**. A further 23 stations yielded correlation coefficients between 0.7–0.9 **in remote tropical or mid-latitude locations**, **predominantly located in remote marine stations across all latitudes and also in polar regions**. The quality of model predictions ($r < 0.5$, 9 stations) is reduced in anthropogenically highly polluted stations in east Asia and the Mediterranean region and stations impacted by peat fire emissions in Indonesia, as local and incidental emissions are 15 difficult to capture. Our H_2 budget corroborates bottom-up estimates in the literature in terms of source and sink strengths and overall atmospheric burden. By simulating hydroxyl radicals (OH) in the atmosphere leading to a CH_4 lifetime in agreement with observationally constrained estimates, we show that the EMAC model is a capable tool for undertaking high accuracy simulation of H_2 at global scale. Future research applications could target the impact of potentially significant natural and anthropogenic H_2 sources on air quality and climate, reducing uncertainties in the H_2 soil sink and impacts of H_2 release on 20 the future oxidising capacity of the atmosphere.



Key figure

1 Introduction

H₂ represents an essential energy vector for 2050 net zero decarbonisation targets to be met. Current demand for H₂ equates to approximately 95 Mt per year with existing uses in the refining industry, as well as the chemical industry for production of 25 ammonia, methanol and other chemicals (Hydrogen Council, 2021; International Energy Agency, 2023). H₂ is also used in the direct reduction of iron along with smaller uses in electronics, glassmaking and metal processing (International Energy Agency, 2023). With increased governmental, financial and policy support, demand for H₂ is forecasted to rise to between 430–690 Mt by 2050 (Hydrogen Council, 2021; International Energy Agency, 2023). Achieving this projected level of hydrogen demand 30 can support clean energy use in: 1) hard to abate sectors such as long-haul trucking, shipping and aviation, 2) sectors that require a clean molecule as a chemical feedstock such as for co-firing of natural gas turbines or industrial processes such as steel manufacturing, 3) sectors that require a source of low carbon heat such as for cement and aluminium production or for buildings (Hydrogen Council, 2021; International Energy Agency, 2023). Use of H₂ offers a lot of potential for securing decarbonisation outcomes, provided clean production pathways are prioritised (Hydrogen Council, 2021; International Energy Agency, 2023), carbon capture and storage technologies (if required) work efficiently and at scale (International Energy Agency, 2020), and 35 leakage rates in the H₂ value chain are minimised with sound engineering design (Esquivel-Elizondo et al., 2023; Fan et al., 2022).

Despite these potential advantages for decarbonisation, H₂ has well-documented climate impacts following its release into the atmosphere which represents an important environmental challenge. In terms of climate impacts, H₂ is an indirect greenhouse gas that leads to increases in radiatively active species by increasing 1) CH₄ lifetime due to H₂ competing for the OH 40 sink 2) tropospheric ozone production due to a chain of reactions initiated by the H atom and 3) stratospheric water vapour that enhances radiative forcing (Derwent et al., 2006; Paulot et al., 2021; Ocko and Hamburg, 2022; Warwick et al., 2022, 2023). Since H₂ release affects the oxidising capacity of the atmosphere, it may also lead to changes in the production of sulphate, 45 nitrate and secondary organic aerosols (Sand et al., 2023). Arising from these modelled results, coupled chemistry-climate modelling has a vital role to play before future H₂ infrastructure is installed to ensure that projected increases in H₂ utilisation do not lead to significant adverse consequences for the earth's atmosphere, air quality and climate.

Simulation of H₂ atmospheric chemistry impacts has attracted significant research attention both in the past few decades (Hauglustaine and Ehhalt, 2002; Schultz et al., 2003; Tromp et al., 2003; Warwick et al., 2004) and at present (Derwent et al., 2020; Paulot et al., 2021, 2024; Warwick et al., 2023) given the likelihood that demand for H₂ usage will grow and potential environmental impacts still require a solution. Previous attempts at simulating hydrogen mixing ratios with coupled chemistry- 50 climate modelling have met variable levels of success at global scale. In this article, we show that the EMAC model is a highly capable tool for capturing 1) the magnitude, amplitude and seasonality of the annual H₂ cycle and 2) the meridional gradients in H₂ mixing ratios. These findings support the conclusion that the EMAC model consistently represents the interplay between the dominating soil sink (i.e. 75% of all sink terms) and atmospheric photochemical production (i.e. 63% of all source terms) which is by far the largest source term for H₂ (Table 2).

55 **2 Materials and methods**

In this work, we employ the EMAC model which couples the 5th generation European Centre Hamburg General Circulation Model (ECHAM5; Roeckner et al. (2003, 2004, 2006)) to the Modular Earth Submodel System (MESSy) (Jöckel et al., 2006, 2010). Simulations were performed with T63 spectral resolution which produces a spatial resolution of 1.9° (approximately 180–190 km). Simulations were performed with 90 levels up to 80 km above the earth's surface, encompassing both 60 the lower and middle atmosphere. Chemical reactions in the atmosphere were modelled with version 1 of the Mainz Isoprene Mechanism (MIM1; Pöschl et al. (2000); Jöckel et al. (2006)). The model experiment ~~covers the time period 2006–2023~~ is ~~representative of the present-day (i.e. the year 2020) and uses meteorology for the years 2006–2023~~, with the first ~~three~~ ~~four~~ years used as spin-up time. Flux boundary conditions were employed for both CH₄ and H₂ to overcome issues with the introduction of artificial sources and sinks arising from using Dirichlet boundary conditions with a prescribed mixing ratio at 65 the lower boundary of the atmosphere. H₂ and CH₄ are chemically coupled and have nearly the same chemical lifetime (Table 1). Both compete for the OH radical as a chemical sink, with OH being by far the dominant sink for atmospheric CH₄ (~~Saunois et al., 2025~~ [Saunois et al. \(2025\)](#); see section 4.1 below). Furthermore, atmospheric oxidation of CH₄ is the largest 70 source for H₂ (Ehhalt and Rohrer, 2009). To adequately simulate such a coupled system, the EMAC model uses flux boundary conditions for sources and sinks of both species. To reach a steady-state for the control simulation, the initial conditions for CH₄ and H₂ were obtained from a 15 years long simulation, covering the period 1990–2005. CH₄ was simulated based on the work of Zimmermann et al. (2020), in which emissions of CH₄ and deposition are represented based on the year 2020. Integration of the equations in the simulation uses a time-step of 450 seconds, and, due to the relatively long lifetime of H₂, precluding diel variability, instantaneous values are outputted every day.

75 **2.1 Emissions**

In this work, the goal is to undertake an equilibrium simulation that reaches steady-state mixing ratios representative of present day atmospheric conditions. Therefore, emissions are based on the year 2020, or the closest year prior to 2020, and are repeated for each year which removes any interannual variability. Due to increasing emissions and its long lifetime CH₄ is not in a steady state. Therefore an equilibrium simulation is not fully representative of the atmospheric state in 2020.

For the long-lived tracer CH₄, the a posteriori emissions and the best combination of the rising-CH₄ scenario of Zimmermann et al. (2020) have been applied. In this work, Zimmermann et al. (2020) show that the EMAC model has been efficient in simulating interactive CH₄ mixing ratios over the last two decades. Therein, the model results compare quite well with NOAA and The Advanced Global Atmospheric Gases Experiment (AGAGE) stations and measurements from CARIBIC (Civil Aircraft for the Regular Investigation of the ~~atmosphere~~ [Atmosphere](#) Based on an Instrument Container) flight observations (Brenninkmeijer et al., 2007). Twelve emission categories are considered here, namely, wetlands other than bogs (SWA), 80 animals (ANI), landfills (LAN), rice paddies (RIC), gas production (GAS), shale gas drilling (SHA), bogs (BOG), coal mining (COA), including minor natural sources from oceans, other anthropogenic sources, volcanoes, oil production and offshore traffic, oil-related emissions (OIL), biomass burning (BIB), termites (TER), and biofuel combustion (BFC). Only emissions 85

from bogs, rice fields, wetlands other than bogs, and biomass burning are subject to seasonal variability. Most of the emissions are based on the emission fields of the Global Atmospheric Methane Synthesis (GAMeS) in which processes with similar isotopic characteristics are aggregated into one group (Houweling et al., 1999). For biomass burning, the GAMeS dataset is replaced by the GFEDv4s (Randerson et al., 2017) and is vertically distributed according to a profile suggested in the EDGAR database (Van Aardenne et al., 2005). The GFEDv4s biomass burning statistics include agricultural waste burning events. A total amount of 601.1 Tg yr^{-1} of CH_4 is emitted in the model and detailed emissions for each sector can be found in Table 1 and 3 of Zimmermann et al. (2020), which also describe in detail the emission optimisation process.

H_2 emissions were taken from the RETRO dataset (Schultz et al., 2008), which was chosen due to its completeness. As for the other sources, we repeated the emissions based on one single year, namely the year 2000. The RETRO database covers the period 1960–2000, and the last year was taken as representative of 2020 emissions, motivated by the stagnation of H_2 emissions in the past few decades (Paulot et al., 2021). A global value of 14.3 Tg yr^{-1} for anthropogenic emissions is obtained from the RETRO database, as well as 4.8 Tg yr^{-1} from soil emissions. Biomass burning emissions were obtained from the GFED (Global Fire Emissions Database) database (Giglio et al., 2013), and accounted for 8.35 Tg yr^{-1} . As the RETRO oceanic emissions are outside the range of emissions suggested by the literature (Paulot et al., 2024), these emissions were upscaled to 3 Tg yr^{-1} so to be within the suggested range (i.e. between $3 - 6 \text{ Tg yr}^{-1}$). Both the RETRO and GFED databases provide direct estimates of H_2 emissions without relying upon an assumed H_2/CO emissions ratio.

For non-GHGs, different emissions were adopted. Anthropogenic sources of short-lived gases are based on CAMS-GLOB-ANTv4.2 and CAMS-GLOB-AIRv1.1 (Granier et al., 2019), and the emissions are estimated with reduction due to lockdowns during the COVID-19 pandemic (Reifenberg et al., 2022). The reduction in the mixing ratio of the OH radical is below 4% for most of the atmosphere, with the exception of the uppermost troposphere and tropopause region, which is due to reduced flight activity. The small impact on OH is foremost confined to [northern hemisphere](#)-mid-latitudes [of the northern hemisphere](#). Biomass burning emissions are calculated online on a daily basis and rely on dry matter burned from observations and fire type (Kaiser et al., 2012). The emission factors for different tracers and fire types are taken from Andreae (2019) and Akagi et al. (2011). The simulation uses a climatology of the aerosol wet surface density to calculate heterogeneous reactions. It is based on the CMIP5 (Climate Model Intercomparison Project Phase 5) emissions climatology for the years 1996–2005 low S scenario (Righi et al., 2013). The aerosol distribution for radiative forcing calculation is the Tanre climatology (Jöckel et al., 2006). The biogenic emissions of organic species have been compiled following Guenther et al. (1995) and are prescribed in the model in an offline manner (Kerkweg et al., 2006), with the exception of biogenic isoprene and terpenes, for which the emissions are calculated online (Kerkweg et al., 2006).

2.2 Soil sink implementation

We estimate the soil sink using a two-layer soil model (Yonemura et al., 2000; Ehhalt and Rohrer, 2013a; Paulot et al., 2021). H_2 is assumed to diffuse through a dry top layer of soil with no bacterial activity (layer I), which may be covered by an equally inactive layer of snow. In a second layer below the top layer (layer II), the rate of H_2 removal by high-affinity hydrogen-oxidising bacteria (Paulot et al., 2021) depends on both soil temperature and moisture. The resulting deposition rate is parameterised by:

$$v_d = \frac{1}{(\delta/D_{\text{soil}}(\theta_{w,I}) + \delta_{\text{snow}}/D_{\text{snow}} + 1/\sqrt{(D_{\text{soil}}(\theta_{w,II}) A g(T) f(\theta_{w,II}/\theta_p))})} \cdot \quad (1)$$

The first two terms in parenthesis in the denominator of Eq. (1) represent diffusion through the inactive soil layer and the
125 snow layer of thickness δ and δ_{snow} , respectively. The diffusivity of H_2 in soil is given by Millington and Quirk (1959):

$$D_{\text{soil}}(\theta_w) = ((\theta_p - \theta_w)^{3.1}/\theta_p^2) D_{\text{air}}, \quad (2)$$

which depends on the volumetric soil water fraction θ_w and the volumetric soil pore fraction (i.e. porosity) θ_p . The diffusivity of H_2 in snow is given by:

$$D_{\text{snow}} = 0.64 D_{\text{air}}, \quad (3)$$

130 while the diffusivity of H_2 in air is given by:

$$D_{\text{air}} = \frac{0.611}{p/1013.25} \frac{((T + 273.15)/273.15)^{1.75}}{p \cdot ((T + 273.15)/273.15)^{1.75}}, \quad (4)$$

where the diffusivity of H_2 in air depends on the air temperature T in $^{\circ}\text{C}$ and the air pressure p in hPa.

The third term in parenthesis in the denominator of Eq. (1) represents H_2 removal in the lower, active layer. The temperature dependence is given by Ehhalt and Rohrer (2011):

$$135 \quad g(T) = \frac{1}{(1 + \exp(-(T - 3.8)/6.7)} + \frac{1}{(1 + \exp((T - 62.2)/7.1)} - 1, \quad (5)$$

where T is the soil temperature in $^{\circ}\text{C}$.

The soil moisture dependence in terms of the water saturation $S = \theta_w/\theta_p$ for eolian sand is given by Ehhalt and Rohrer (2011):

$$f_{\text{es}}(S) = 0.00936 \frac{(S - S_{\text{es}}^*)(1 - S)}{S^2 - 0.1715S + 0.03144}, \quad (6)$$

140 where $S_{\text{es}}^* = 0.02640$ is the minimum level of water saturation required for microbial activity. For loess loam the soil moisture dependency is given by Ehhalt and Rohrer (2011):

$$f_{\text{ll}}(S) = 0.01997 \frac{(S - S_{\text{ll}}^*)(0.8508 - S)}{S^2 - 0.7541S + 0.2806}, \quad (7)$$

where $S_{\text{ll}}^* = 0.05369$. For a mixture of eolian sand and loess loam we use the weighted mean given by:

$$f(S) = \varphi_{\text{sand}} f_{\text{es}}(S) + (1 - \varphi_{\text{sand}}) f_{\text{ll}}(S), \quad (8)$$

145 where φ_{sand} is the sand fraction of the soil.

The resolution-dependent constant A represents bacterial activity and is adjusted to yield a global mean deposition velocity of

0.033 cm s⁻¹ over land during 2012 to 2015 (Yashiro et al., 2011). Using the 0.25° grid spacing of the ERA5 input data, we obtain $A = 10.9$.

The thickness of the upper soil layer without hydrogenase (i.e. an enzyme in prokaryotes such as bacteria that consume H₂) activity is parametrised by:

$$\delta_s = 0.0057((\theta_p - \theta_w)/\theta_w)^{2.5}, \quad (9)$$

in sandy loam and

$$\delta_l = 0.109((\theta_p - \theta_w)/\theta_w)^{1.8}, \quad (10)$$

in loam. Both δ_s and δ_l are expressed in cm. For a mixture of sandy loam and loam with sand fraction φ_{sand} we use the weighted mean to calculate the soil layer thickness via:

$$\delta = \varphi_{\text{sand}}\delta_s + (1 - \varphi_{\text{sand}})\delta_l. \quad (11)$$

The soil water content in the top, dry layer (i.e. θ_{wI}) is assumed to be the threshold moisture content below which the bacterial activity vanishes, i.e. there is no H₂ uptake in this layer, and is given by:

$$\theta_{wI} = S^* \theta_p, \quad (12)$$

where $S^* = S_{\text{es}}^*$ is the threshold moisture content for eolian sand and $S^* = S_{\text{ll}}^*$ for loess loam.

Accordingly, the remaining water within the top 10 cm of soil is between depth δ and 10 cm, resulting in a soil water content for the second layer (i.e. θ_{wII}) of:

$$\theta_{wII} = \frac{10\theta_w - \delta\theta_{wI}}{10 - \delta}. \quad (13)$$

We evaluated Eq. (1) using monthly reanalysis data for soil moisture, soil temperature, air pressure, snow depth and snow density with a 0.25° grid spacing from the ERA5 dataset provided by the European Centre for Medium-Range Weather Forecasts (ECMWF) (Hersbach et al., 2020, 2023). The mean soil moisture and soil temperature for the top 10 cm soil layer was obtained by linearly interpolating the ERA5 soil level data. The volumetric soil water content was then uniformly reduced by 6% (Paulot et al., 2021). Static soil porosity and sand fraction maps with 0.25° grid spacing were obtained from the Land Data Assimilation System (LDAS) (Rodell et al., 2004; GLDAS, 2024).

The global distribution of the H₂ deposition velocity averaged over the 2012 to 2021 period resembles the maps presented by Paulot et al. (2021), but with more pronounced extrema (Figure S1 in the supplement). The zonal mean of the H₂ deposition velocity over land also falls within the range of results reported by Paulot et al. (2021). However, the local minimum around 20°N, due to the Sahara, and the maximum around 10°N, where the transition to more humid regions favours soil uptake, are more distinct in this study than in most of those shown by Paulot et al. (2021) (Figure S2 in the supplement). Thanks to extensive observational records of atmospheric hydrogen concentrations at stations around the world, it is possible to carry out detailed validation of hydrogen deposition based on the resulting concentrations. This method, presented in the following sections, is more informative than local deposition analysis because it is less susceptible to significant variations in surface conditions and is based on a much larger database.

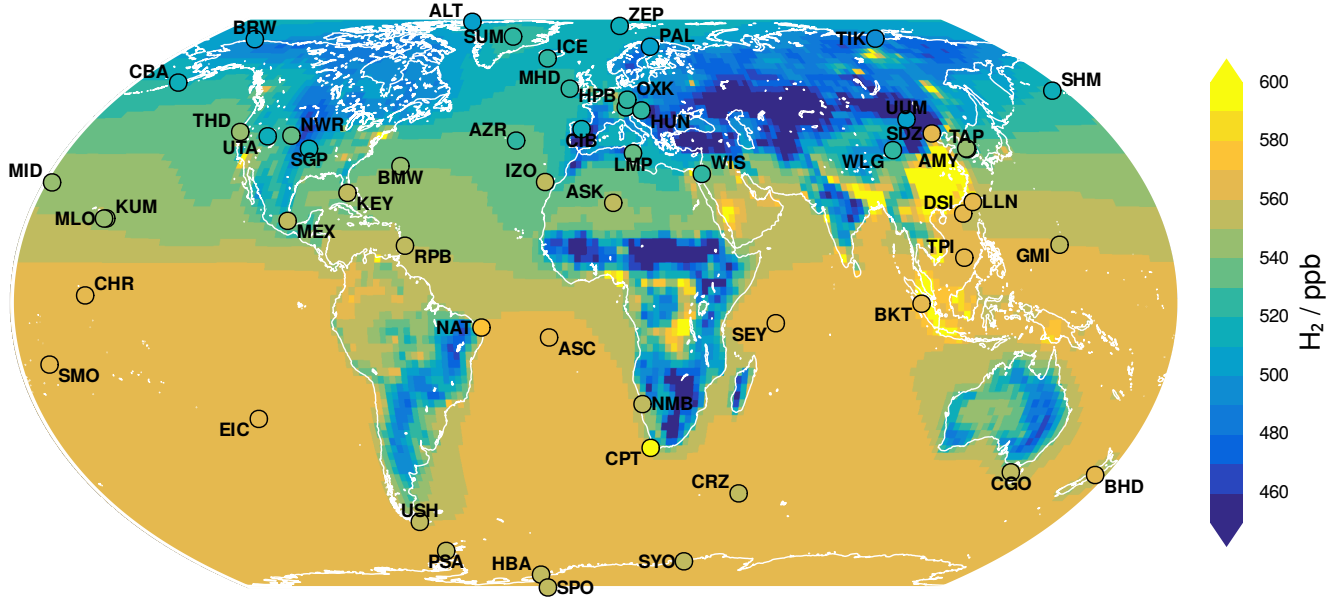


Figure 1. Global map of H_2 mixing ratios and the location of observational stations. Model data is averaged over the years 2010–2023 (inclusive) which is representative of the year 2020 for a steady-state simulation, while observational data uses mid-2020 values from a detrending fit using a sixth order harmonic regression technique.

2.3 Observations

180 EMAC simulations are compared with observational data from 56 stations (with more than 12 monthly values) that form part of the NOAA GML Carbon Cycle Cooperative Global Air Sampling Network (Petron et al., 2024). Data gaps exist at some stations due to the application of quality control procedures, as well as missing data due to impacts of the COVID-19 pandemic. For comparison with the results of the EMAC equilibrium simulation, the observed monthly values have been detrended by subtracting the trend obtained by a sixth order harmonic regression with a linear trend term, while keeping the mid-year values
185 for 2020 fixed.

3 Results

Figure 1 presents a global map of modelled annual mean H_2 mixing ratios as well as the location of observational stations that we use for model inter-comparison purposes. This global map shows the inter-hemispheric gradient for this molecule whereby H_2 mixing ratios are higher in the southern hemisphere compared to the northern hemisphere. This global map also shows the
190 influence of pollution hotspots in Asia, and the influence of biomass burning emissions in central Africa and peat fire emissions in southeast Asia.

We show time series data for model comparisons with observational data (without gaps in monthly data) from 20 observational stations in Fig. Figure 2. Further comparisons with observational data from another 36 observational stations (with data gaps) are shown in Fig. Figures B1 and B2. 38 of the 56 stations have marine characteristics (Table A1 and Figure 1), i.e. are located coastally or on islands. 11 stations can be described as polar (latitude $> 60^\circ$), and 14 stations are positioned on mountains (i.e. a single station might have several characteristics). These stations usually measure remote, often marine air masses or free tropospheric concentrations. Just 8 stations Hungary (HUN), Mongolia (UUM), CIBA (CIB, northern central Spain), Shangdianzi (SDZ, China), Wendover (UTA, Utah), Southern Great Plane (SGP, Oklahoma), Israel (WIS), and Gobabeb (NMB, Namibia) fall in none of these previous categories. Inner continental non-mountain stations are sparse, with none in South America and Australia. The two continental stations in Africa (ASK, and NMB) are located in the desert. There are also no monitoring stations in Central Asia. The three Mediterranean stations (CIB, LMP, and WIS) and the continental Chinese (SDZ) and Mongolian (UUM) stations are located in or close to areas with high air pollution levels (Lelieveld et al. (2002); Silver et al. (2025)). The Bukit station (BKT, Indonesia) is also regularly impacted by biomass burning and peat fires Yokelson et al. (2022).

Across these 56 observational stations, the Pearson correlation coefficient (r) exceeds 0.9 for eight stations that experience well-mixed unpolluted air masses. Such stations are either remote or located at high latitude in either remote stations located either in the Arctic or Antarctic regions and on islands at high mid-latitudes. In such cases, the annual cycle of H_2 is modelled excellently in terms of magnitude, amplitude and seasonality. In contrast, the nine stations produce correlation coefficients below 0.5. The three stations in the Mediterranean region; namely, Lampedusa (LMP, 0.04), CIBA in northern central Spain (CIB, -0.17) and Israel (WIS, CIB (-0.17), LMP (0.05) and WIS (-0.29) produce and the Chinese and the Mongolian stations SDZ (-0.2) and UUM (0.03) show correlation coefficients close to zero or even negative. The same holds for two stations located in Shangdianzi (China, SDZ, -0.2) and Ulaan Uul (Mongolia, UUM, 0.03). The EMAC model is under performing at Negative r values suggest that the EMAC model does not correctly capture the phasing of the annual H_2 cycle which results in pronounced phase mismatches or anti-correlation in Table B1 and Figures 2, B1, and B2. These stations are located in regions known for high levels of air pollution. The two tropical coastal stations, Natal (Brazil, NAT) and Bukit (Indonesia, BKT) with correlation coefficients of BKT (0.14) and the Natal station in Brazil (NAT, 0.14 in contrast) do show rather low r values compared to other tropical stations. These stations are located in regions that do not experience well-mixed unpolluted air masses (e.g. Mediterranean region, UUM, SDZ) or are They are impacted by biomass burning (i.e. NAT) and peat fire emissions (i.e. BKT). Negative The comparison at the Hungarian station (HUN, 0.39) shows a considerably lower r values suggest that the EMAC model does not correctly capture the phasing of the annual H_2 cycle which results in an anti-correlation in Table B1 value compared to the other two central European stations Hohenpeissenberg (HPB, 0.56) and Ochsenkopf (OXK, 0.64). HPB and OXK are mountain stations less susceptible to local mismatches in H_2 soil deposition, as can be seen from the much better matching of model amplitude and phasing with measurements. The Christmas Island station (CHR, 0.43) is the only very remote tropical island station, which has a considerably low r value. At this station, the observational time series is relatively short with hardly any annual cycle. Another 23 stations have correlation coefficients between 0.7–0.9 which demonstrate very good agreement between model and observational data. A number of these stations are located in the mid-

latitudes either in the northern or southern hemisphere. The remaining 48–16 stations produce correlation coefficients between 0.30.5–0.7 mostly in either remote tropical or mid-latitude regions. Especially the Antarctic stations show an upward trend for atmospheric H₂. The model with its emissions and soil sink repeating the year 2020, cannot capture this feature. This trend 230 coincides with further increasing atmospheric CH₄ concentrations after 2010 following its hiatus of the previous decade (Lan et al., 2024). Table 2 shows that oxidation of atmospheric CH₄ is the largest source term for H₂ Ehhalt and Rohrer (2009). To investigate this further in the future, a model simulation with flux boundary conditions for H₂ and CH₄ in transient mode is 235 needed. Overall, the results are very promising and demonstrate the ability of the EMAC model to predict H₂ mixing ratios accurately in most regions of the earth. To provide a visual overview of these results, Fig.–Figure 3 provides a global map of Pearson correlation coefficients for comparison of EMAC and observational data.

We also present a plot of the meridional gradient in H₂ in Fig.–Figure 4. Overall, meridional gradients in H₂ are captured 240 very well by the EMAC model, notably for stations located in the southern hemisphere, likely because many represent the background atmosphere, whereas many stations in the northern hemisphere are affected by local influences. The model correctly predicts higher H₂ mixing ratios in the southern hemisphere even though the majority of H₂ sources are present in the northern hemisphere. The predicted interhemispheric gradient in H₂ presented here is correct by virtue of the greater soil sink 245 that is present in the northern hemisphere arising from its larger land area (Ehhalt and Rohrer, 2009). Most of the discrepancies between the observed and predicted H₂ mixing ratios exist for a small number of stations within the northern hemisphere mid-latitudes (between 30–60° N) and in the tropics, presumably influenced by local source variability that is insufficiently resolved by our global model. The coverage of many continental land masses by the observational stations is sparse. For South 250 America, Australia, Africa, Central Asia, Siberia and India there are almost no measurements available. This is a problem, especially in validating the soil sink, which can be considered the most uncertain part of the H₂ budget (Paultot et al., 2021).

For further results, we refer the reader to Appendix B which provides further graphs and tabulated summaries of model performance.

4 Discussion

250 4.1 Model comparison with observational data

A key feature of the results (Fig.–2, Fig.–B1 and Fig.–Figures 2, B1, and B2) is the ability of the EMAC model to realistically 255 predict the magnitude, amplitude and seasonality of the annual H₂ cycle at most stations, in unison with that from CH₄ Zimmermann et al. (2020), with both compounds being modelled with flux boundary conditions and interactive sinks. Promising results are obtained especially for stations that experience well-mixed unpolluted remote air masses, for example, in mostly polar regions, which are particularly sensitive to atmospheric transport and chemistry dynamics. The EMAC model results are also quite promising in a range of mid-latitude stations both in the northern and southern hemisphere. In contrast, there are some regions of the globe (Fig.–Figure 3) where results are not as promising. For example, the EMAC model predictions are less accurate in the highly anthropogenically polluted Mediterranean region, near the Amazonian region which is impacted by biomass burning emissions, and southeast Asia which is impacted by peat fire emissions. Due to the coarse spatial resolution of

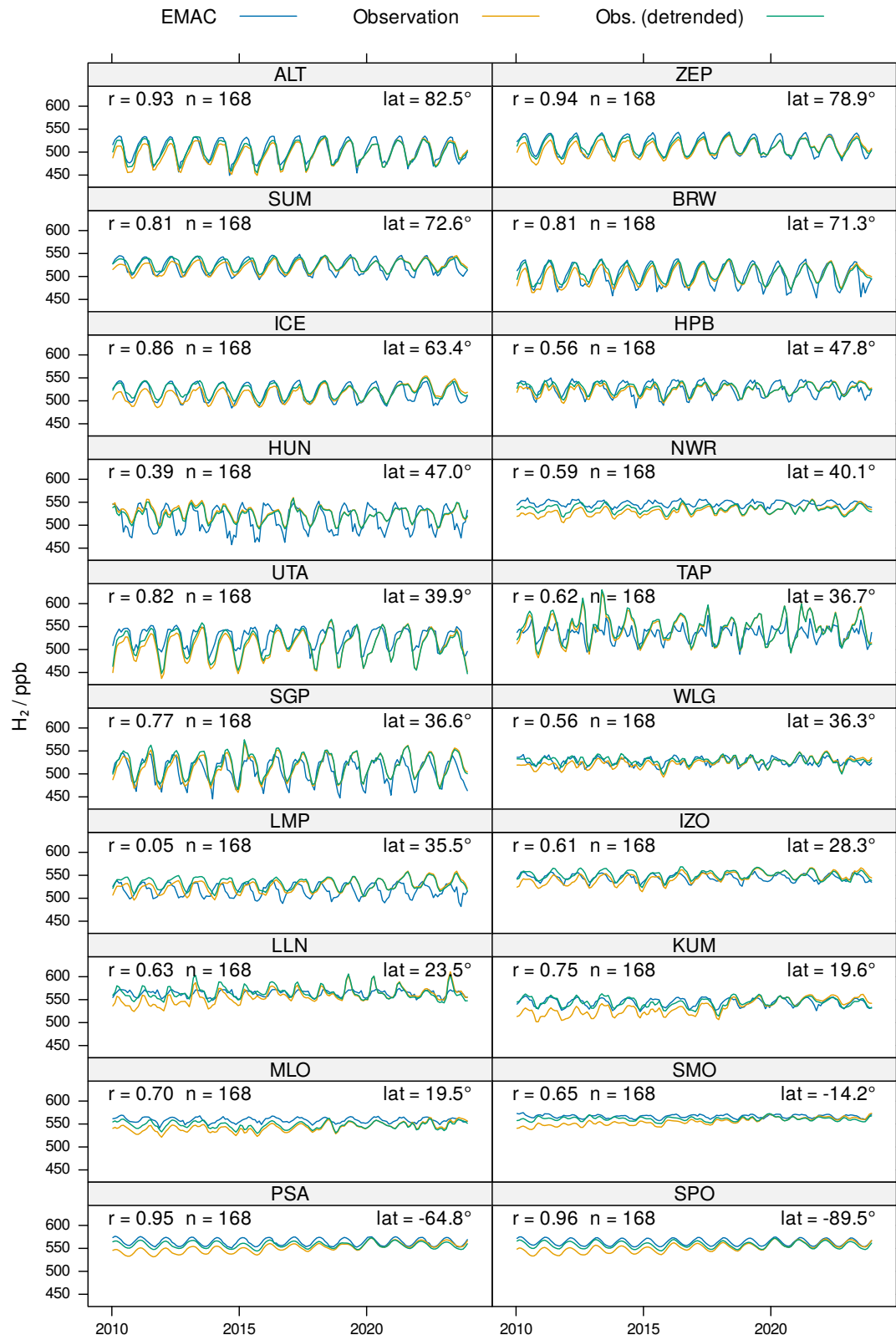


Figure 2. Time series comparison of observational and EMAC model data for H₂. Results are presented for 20 stations without any gap in monthly data. The sample size for observational data is denoted by n , while r is the Pearson correlation coefficient. Latitudes are denoted by lat .

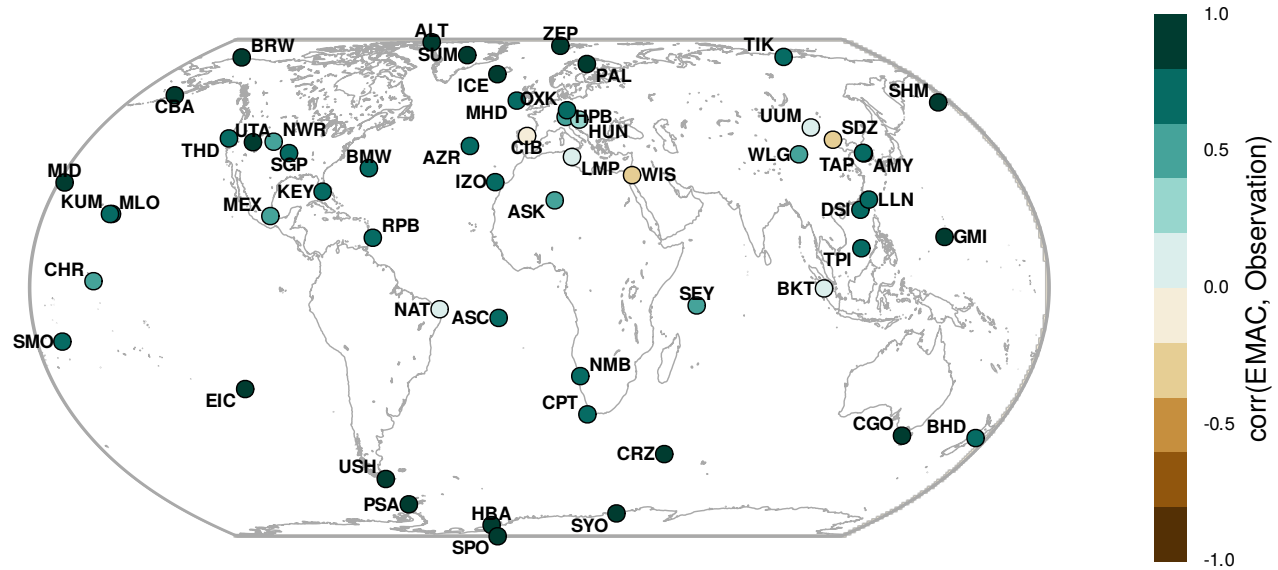


Figure 3. Pearson correlation coefficient for the intercomparison between EMAC and observational data for H₂. Model data is compared with detrended observational data for the years 2010–2023 (inclusive) to perform this calculation.

260 180–190 km and limited information about local and incidental sources, the variability of mixing ratios in these regions is more challenging to capture. This is especially the case for some coastal stations (e.g. NAT, BKT) where the model is limited due to resolution in accurately representing the mixing of marine and continental air. Also the deviations in China and Mongolia (SDZ, UUM) can be partly attributed to a resolution effect. Both stations are located close to strong horizontal gradients in H₂ mixing ratios. The vertical resolution of the lowermost model layers (i.e. thicknesses of 66 m, 166 m and 319 m from the surface upwards) and the representation of the orography influence the comparison. It is important to consider the measurement height relative to the surface and the geographic prominence of the stations. For example, the modelled amplitude of the annual H₂ cycle can be reduced by up to 40% between the surface and the next model layer for continental stations due to the importance of the soil sink, whereas the H₂ mixing ratios increase with height driven by the strong atmospheric chemical H₂ production. In addition, an interesting model-measurement discrepancy occurs at the Weizmann Institute of Science (WIS) station near the 265 northern Red Sea, where unaccounted for alkane emissions have been attributed to natural seepage from deep water sources (Bourtsoukidis et al., 2020), possibly accompanied by H₂ emissions. Overall, the EMAC model performs favourably at a global scale for simulating H₂ mixing ratios. Comparison with model output from Yashiro et al. (2011) shows that while the EMAC model produces correlation coefficients in excess of 0.7 for over half of the observational stations, the CHASER chemistry-climate model achieves the same result for only one quarter of all observational stations. The annual mean H₂ mixing ratios 270 are well captured by the EMAC model (Table B1 and Fig. Figure 4), with the exception of CIB ($r=-0.17$), UUM ($r=0.03$),

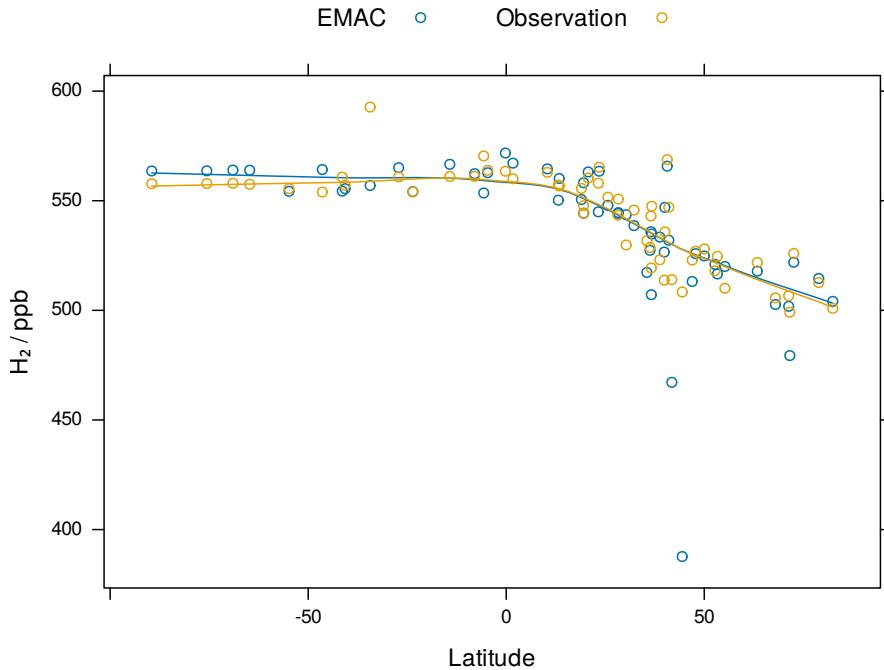


Figure 4. Meridional gradients in H_2 for EMAC predictions and observational data where stations had more than 12 monthly values. The solid lines were obtained by locally estimated scatterplot smoothing (LOESS; smoothing parameter 2 / 3, locally linear). Negative latitudes represent south and positive latitudes represent north of the equator. Data are shown for stations with more than 12 monthly values.

and the coastal station Cape Town (CPT) despite its high Pearson correlation coefficient ($r=0.73$). As mentioned above, the H_2 observational stations do not represent the inner region of continents well. Especially, the small number (UTA, SGP, UUM) of remote non-mountain, non-hyperarid stations, placed away from highly anthropogenically influenced regions limits its usage in looking in more detail on the parametrisation of the soil sink. At Wendover (UTA, Utah, arid cold climate, $r = 0.82$) and the Southern Great Plains (SGP, Oklahoma, humid subtropical climate, $r = 0.77$), shown in Figure 2, the model performs well by realistically representing the magnitude, amplitude and seasonality of the observations, indicating that the soil sink parametrisation of H_2 is realistic in those regions. The poor results at the Mongolian station (UUM, arid cold climate, $r = 0.03$), Figure B1, might be partly attributed to a resolution effect (see above).

280

To successfully simulate H_2 mixing ratios in the atmosphere, a model needs to correctly resolve the complex interplay between meteorology and chemistry. In terms of chemistry, having the oxidising capacity of the atmosphere represented correctly is a key consideration (Prather and Zhu, 2024). It is largely controlled by the concentration of OH radicals in the troposphere (Lelieveld et al., 2016) and determines the atmospheric lifetime of numerous species including CH_4 . The total CH_4 sink is largely dominated by its reaction with OH (see Saunois et al. (2025) for a review). In this sense, CH_4 lifetime is a measure for the total oxidative capacity of the atmosphere. Observational estimates derived from methyl chloroform (CH_3CCl_3) measurements lead to a total atmospheric CH_4 lifetime of 9.1 ± 0.9 years (Prather et al., 2012). Our estimate of 9.3 ± 0.06 years

(Table 1) compares well, and is only marginally higher than the range indicated by Prather et al. (2012). This also holds for the global tropospheric chemical CH₄ sink. The supporting information of Prather et al. (2012) states that for the tropospheric CH₄ lifetime based on the reaction with OH (i.e. 11.2 ± 1.3 years) and for the lifetime of CH₄ based on the reaction with tropospheric chlorine (i.e. 200 ± 100 years) yields a combined tropospheric chemical lifetime of 10.6 ± 1.2 years for CH₄. This
295 value compares quite well with our estimate of 10.4 years (Table 1). Model intercomparisons performed by Nicely et al. (2020) suggests that many chemistry models underestimate CH₄ lifetime due to simulating an atmosphere that is overly enriched in OH radicals. Recently, work by Yang et al. (2025) concurs that several atmospheric chemistry models over-predict OH mixing ratios which has implications for CH₄ and H₂ lifetimes. The multi-model estimate from CMIP6 (Coupled-Model Intercomparison Project 6; Collins et al. (2017)) and CCMCI (Chemistry Climate Model Initiative; Plummer et al. (2021)) models used by
300 the Global Carbon Project community for the bottom-up estimates of CH₄ sources yields a total CH₄ lifetime of 8.2 years with a range of 6.8–9.7 years (Saunois et al., 2025). It also shows a large spread, which propagates into increased uncertainties for the derivation of emission budgets. We believe that the EMAC model is realistically capturing the total oxidising capacity of the atmosphere which helps to facilitate high-accuracy prediction of H₂ and CH₄ dynamics.

4.2 Budget and lifetimes

305 In the atmosphere, CH₄ and H₂ are tracers strongly connected with similar chemical fates. Table 1 shows that CH₄ and H₂ have nearly identical chemical lifetimes both in the troposphere and atmosphere. Furthermore the total sources of H₂ and CH₄, corrected for molecular masses, are very comparable. The biggest difference between these two compounds stems from hydrogen's much larger soil sink which reduces its tropospheric lifetime by approximately a factor of four compared to CH₄.

310 In Table 2, we compare our H₂ budget derived from EMAC model output with other estimates from the literature. We find that our H₂ budget agrees favourably with bottom-up literature estimates that rely on a combination of emission datasets and model calculations of turnovers and loss rates, but differs from top-down estimates relying on either inverse modelling (Xiao et al., 2007) or analysis of the ²H (i.e. deuterium) budget (Rhee et al., 2006). Our overall budgeting of sources and sinks agrees very well with bottom-up estimates. In addition, our tropospheric H₂ lifetime is in very good agreement with bottom-up estimates. The tropospheric burden is in the upper range of model estimates. Note, that the upper boundary of the tropospheric
315 range is often not clearly defined in the literature, with different definitions e.g. 100 hPa, World Meteorological Organization (WMO), or a climatological tropopause being used. In this study the WMO tropopause definition is used based on a dynamic tropopause in high latitudes and lapse rate being used at low latitudes. The photochemical production is in between the range for bottom-up and top-down estimates (Paulot et al., 2021). These findings suggest that the EMAC model simulates a realistic atmospheric oxidation capacity which is a critical requirement for predicting H₂ mixing ratios well.

320 Recent work by the United States Geological Survey (Ellis and Gelman, 2024) has developed a simple, zero-dimensional mass balance model coupled with Monte Carlo uncertainty analysis to explore global potential for geological (or gold) H₂ production in the earth's crust. Median modelled estimates of the subsurface H₂ resource are approximately 5.6×10^6 megatonnes. Ellis and Gelman (2024) estimate that global geological H₂ resources cause an additional global flux of 24 Tg yr^{-1} from the subsurface to the atmosphere. This is speculative and would add unaccounted H₂ emissions almost of the strength

325 of the current non-photochemical sources. Current knowledge concerning the budget of atmospheric H₂ does not exclude the existence of a large geological H₂ reservoir, and further emphasises the importance of dry deposition for the global atmospheric H₂ budget.

Table 1. Chemical budgets and lifetimes for H₂ and CH₄. Uncertainties are calculated as the standard deviation of multi-year annual global means. Note that lifetimes are always calculated with respect to global burden (Prather et al., 2012; SPARC, 2013).

Budget term	H ₂	CH ₄
Tropospheric chemical sink (Tg yr ⁻¹)	19.0 ± 0.16	534.5 ± 4.04
Tropospheric chemical production (Tg yr ⁻¹)	49.5 ± 0.43	-
Tropospheric chemical lifetime (years)	10.5 ± 0.08	10.4 ± 0.08
Atmospheric chemical lifetime (years)	9.6 ± 0.07	9.8 ± 0.07
Soil sink (Tg yr ⁻¹)	60.5 ± 0.07	30.9 ± 0.02
Tropospheric lifetime (years)	2.5 ± 0.004	9.9 ± 0.07
Atmospheric lifetime (years)	2.5 ± 0.004	9.3 ± 0.06

4.3 Suggestions for future applications

Future research efforts in modelling H₂ atmospheric chemistry could build on the current work in three key ways. Firstly, scenarios could be constructed to explore what role geological H₂ (i.e. gold H₂) holds for future atmospheric chemistry. If economically extractable reserves of gold H₂ are found, future utilisation of H₂ would increase well beyond current projections (Hand, 2023; Truche et al., 2024; Ellis and Gelman, 2024). It would therefore be critical to assess the atmospheric chemistry implications of vastly increased H₂ usage. Secondly, it will be critical to assess what impact H₂ use has on the future oxidising capacity of the atmosphere. Clean H₂ use will be associated with significant reductions in the co-emission of criteria pollutants (Galimova et al., 2022) which will influence the formation of atmospheric oxidants such as ozone and OH radicals that constrain CH₄ and H₂ lifetimes (Archibald et al., 2011; Brasseur et al., 1998; Ganzeveld et al., 2010). Thirdly, the H₂ budget is dominated by the land sink (Tables 1 and 2) and future research efforts could help to constrain the important role played by a number of soil properties (e.g. porosity, soil moisture, temperature, and organic carbon content) on terrestrial H₂ uptake (Ehhalt and Rohrer, 2011, 2013a; Paulot et al., 2021; Smith-Downey et al., 2006). The production of H₂ by enzymes in soil (i.e. hydrogenases) could also be considered in a depth-resolved manner as knowledge of the underlying processes improves (Ehhalt and Rohrer, 2013b). Recent coupling of the JSBACH vegetation model to EMAC by Martin et al. (2024) has developed a potential model tool for undertaking on-line H₂ land sink calculations.

Table 2. Tabulation of the H₂ budget from this study and from literature estimates. Uncertainties are calculated as the standard deviation of multi-year annual means.

Budget term	This study (EMAC)	Seiler and Conrad (1987)	Warneck (1988)	Novelli et al. (1999)	Hauglustaine and Ehhalt (2002)	Sanderson et al. (2003)	Rhee et al. (2006)	Price et al. (2007)	Xiao et al. (2007)	Ehhalt and Rohrer (2009)	Pieterse et al. (2011)	Yashiro et al. (2011)	Paulot et al. (2021)	Sand et al. (2023) ^c	Paulot et al. (2024)
Sources: Tg yr⁻¹															
Tropospheric	79.1 ± 0.4	87 ± 38	89	77 ± 16	70	78.2	107 ± 11	73	76 ± 14	77.3	73–80	74.4	74–102	74 ± 1	
Photochemical	49.5 ± 0.4	40 ± 15	50	40 ± 16	31	30.2	64 ± 12	34.3	41 ± 11	37.3	38–39	42.1	34–56	44	
CH ₄ oxidation	34.5 ± 0.4	15 ± 5	29	26 ± 9		15.2		24.5		23 ± 8				27	
VOC oxidation	15.0 ± 0.2	25 ± 10	21	14 ± 7		15		9.8		18 ± 7				17	
Direct	29.6	47	39	37	39	48	43	38.8	27	35	40	30–37	32.3	23–68	30
Ocean	3 ^a	4 ± 2	4	3 ± 2	5	4	6 ± 5	6 ± 3	6 ± 3	5	5	6	6	6	6
Biofuel								4.4							
Soil	4.8	3 ± 2	3	3 ± 1	5	4	6 ± 5	0	3 ± 2	3	3	3	3	3	3
Biomass															
burning	7.5	20 ± 10	15	16 ± 5	13	20	16 ± 3	10.1	12 ± 3	15 ± 6	15	8–15	9		8
Anthropogenic	14.3	20 ± 10	17	15 ± 10	16	20	15 ± 6	18.3	15 ± 10	11 ± 4	17	15.1–15.4	14.3		13
Atmospheric	81.1 ± 0.4								103 ± 10						
Photochemical	51.5 ± 0.4								76 ± 9						
Stratospheric CH ₄ oxidation	1.94 ± 0.02														
Stratospheric VOC oxidation	0.08 ± 0.02														
Sinks: Tg yr⁻¹															
Troposphere	81.2 ± 0.2	98 ± 23	89	75 ± 41	70	75.4	107 ± 11	73	103.9	79	77.9	75–78	75.1	75–102	
Soil uptake	60.5 ^b ± 0.1	90 ± 20	78	56 ± 41	55	58.3	88 ± 11	55 ± 8.3	84 ± 8	60	55.8	57–60 ± 12	54.7	44–73	
Photochemical	20.8 ± 0.2	8 ± 3	11	19 ± 5	15	17.1	19 ± 3	18	19.9	19	22.1	17–18	20.4	22–30	
Troposphere	19.0 ± 0.2								18 ± 3						
Stratosphere	1.8 ± 0.01								1.9 ± 0.3						
Burden: Tg	199.6 ± 0.2								191 ± 29					184–209	
Stratosphere	34.4 ± 0.1								42						
Troposphere	165.2 ± 0.3	163	155 ± 10	136	172	150	141	149 ± 23	155 ± 10	169	148–153	157.4			
IHD (ppbv)	29.4 ± 0.4														
Lifetime (years)	2.1 ± 0.003		1.8	2.1	1.9	2.2	1.4	1.9	1.4 ± 0.2	2	2.2	1.9–2.0	2.1	1.9–2.7	2.5

^a Up-scaled from 0.5 to 3 Tg/yr to match literature recommendations (Paulot et al., 2021); ^b the dry deposition velocity of H₂ Paulot et al. (2021) has been reduced by 6% (from the continental global mean of 0.035 to 0.033 cm s⁻¹ to improve simulated H₂ especially in polar latitudes. ^c Multi-model results are presented as a range. VOC = volatile organic compound. IHD = interhemispheric difference.

5 Conclusions

In this study, we have successfully extended and used the EMAC model to undertake simulations of H₂ atmospheric dynamics, constrained by flux boundary conditions for both H₂ and CH₄. Comparing the EMAC model output with observational data at 56 stations from the NOAA GML Carbon Cycle Cooperative Global Air Sampling Network generally indicates very good agreement at global scale. Excellent results are achieved at [observational stations that experience well-mixed unpolluted air masses](#) [remote observational stations and for stations measuring remote and free tropospheric air](#), suggesting that atmospheric source, sink and transport processes are accurately represented, while model performance is degraded at stations impacted by nearby pollution sources. Our H₂ budget is also in good agreement with bottom-up estimates in the literature. We find that

the EMAC model simulates the CH₄ chemical lifetime in excellent agreement with observational estimates, which suggests the model calculates OH radical mixing ratios in a representative manner. The H₂ soil sink, based on a two-layer soil model (Yonemura et al., 2000; Ehhalt and Rohrer, 2013a; Paulot et al., 2021), in combination with monthly ERA5 reanalysis data for soil related parameters has been successfully used by the EMAC model. We conclude that atmosphere chemistry models with 355 such features, capturing the most dominant terms of the atmospheric H₂ budget, should be able to generally simulate station observations of atmospheric hydrogen. This gives confidence that scenario simulations regarding the future H₂ economy will provide reliable estimates of its atmospheric impact.

Code and data availability. The Modular Earth Submodel System (MESSy) is in continuous development and is used by a consortium of institutions. Source code access and usage is licensed to all affiliates of institutions which are members of the MESSy Consortium. 360 Institutions can become a member of the MESSy Consortium by signing the MESSy Memorandum of Understanding. The MESSy Consortium website (<http://www.messy-interface.org>) provides further information regarding access to the model. The exact version of the EMAC v2.55.2 source code and simulation set-ups used to produce the results used in this paper is archived on the Zenodo repository at <https://doi.org/10.5281/zenodo.15211346> (The MESSy Consortium, 2025).

Regarding data availability, access to the NOAA GML Carbon Cycle Cooperative Global Air Sampling Network data is available at 365 <https://doi.org/10.15138/WPOW-EZ08> (Petron et al., 2024), the ERA5 reanalysis data is available at <https://doi.org/10.24381/cds.adbb2d47> (Hersbach et al., 2023), and the Global Fire Emissions Database (GFED) v4.1 data is available at <https://doi.org/10.3334/ORNLDAAC/1293> (Randerson et al., 2017). The monthly H₂ deposition velocity at 0.25° resolution is available from the Edmond Open Research Data Repository of the Max Planck Society (Klingmüller, 2025).

Appendix A: List of observational stations

Table A1. Observational Stations from the NOAA GML Carbon Cycle Cooperative Global Air Sampling Network. The station code is complemented with p for polar (latitude $\geq |60^\circ|$), ma for marine i.e. coastal/island, and m for mountain for further characterisation.

height	Station code	Station Name	Latitude	Longitude	Elevation (masl)	Country	Cooperating Agencies
ALT 		Alert, Nunavut	82.4508° North	62.5072° West	185	Canada	Environment Canada
AMY 		Anmyeon-do	36.5389° North	126.3295° East	47	Republic of Korea	Korea Global Atmosphere Watch Center, Korea Meteorological Administration
ASC 		Ascension Island	7.9667° South	14.4° West	85	United Kingdom	Met Office (United Kingdom)
ASK 		Assekrem	23.2625° North	5.6322° East	2710	Algeria	Office National de la Meteorologie
AZR 		Terceira Island, Azores	38.766° North	27.375° West	19	Portugal	Instituto Nacional de Meteorologia e Geofisica
BHD 		Baring Head Station	41.4083° South	174.871° East	85	New Zealand	National Institute of Water and Atmospheric Research
BKT 		Bukit Kototabang	0.202° South	100.318° East	845	Indonesia	Bureau of Meteorology and Geophysics
BMW 		Tudor Hill, Bermuda	32.2647° North	64.8788° West	30	United Kingdom	Bermuda Institute of Ocean Sciences
BRW 		Barrow Atmospheric Baseline Observatory	71.323° North	156.6114° West	11	United States	NOAA Global Monitoring Laboratory
CBA 		Cold Bay, Alaska	55.21° North	162.72° West	21.34	United States	U.S. National Weather Service
CGO 		Cape Grim, Tasmania	40.683° South	144.69° East	94	Australia	CSIRO
CHR 		Christmas Island	1.7° North	157.1518° West	0	Republic of Kiribati	Dive Kiribati
CIB		Centro de Investigacion de la Baja Atmosfera (CIBA)	41.81° North	4.93° West	845	Spain	Centro de Investigacion de la Baja Atmosfera, University of Valladolid
CPT 		Cape Point	34.5523° South	18.4891° East	230	South Africa	South African Weather Service
CRZ 		Crozet Island	46.4337° South	51.8478° East	197	France	Centre des Faibles Radioactivities/TAAF
DSI 		Dongsha Island	20.6992° North	116.7297° East	3	Taiwan	National Central University, Taiwan
EIC 		Easter Island	27.1597° South	109.4284° West	47	Chile	Direccion Meteorologica de Chile
GMI 		Mariana Islands	13.386° North	144.656° East	0	Guam	University of Guam/Marine Laboratory
HBA 		Halley Station, Antarctica	75.55° South	25.63° West	30	United Kingdom	British Antarctic Survey
HPB 		Hohenpeissenberg	47.8011° North	11.0245° East	985	Germany	Deutscher Wetterdienst
HUN		Hegyhatsal	46.9559° North	16.6521° East	248	Hungary	Hungarian Academy of Sciences
ICE 		Storhofdi, Vestmannaeyjar	63.3998° North	20.2884° West	118	Iceland	Icelandic Meteorological Office
IZO 		Izana, Tenerife, Canary Islands	28.309° North	16.499° West	2372.9	Spain	Izana Observatory/Meteorological State Agency of Spain
KEY 		Key Biscayne, Florida	25.6654° North	80.158° West	1	United States	NOAA Atlantic Oceanographic and Meteorological Laboratory
KUM 		Cape Kumukahi, Hawaii	19.5608° North	154.8883° West	8	United States	NOAA Global Monitoring Laboratory
LLN 		Lulin	23.47° North	120.87° East	2862	Taiwan	Lulin Atmospheric Background Station
LMP 		Lampedusa	35.5181° North	12.6322° East	45	Italy	Ente per le Nuove tecnologie, l'Energia e l'Ambiente
MEX 		High Altitude Global Climate Observation Center	18.9841° North	97.311° West	4464	Mexico	Sistema Internacional de Monitoreo Ambiental
MHD 		Mace Head, County Galway	53.326° North	9.899° West	5	Ireland	National University of Ireland, Galway
MID 		Sand Island, Midway	28.2186° North	177.3678° West	4.6	United States	U.S. Fish and Wildlife Service
MLO 		Mauna Loa, Hawaii	19.5362° North	155.5763° West	3397	United States	NOAA Global Monitoring Laboratory
NAT 		Farol De Mae Luiza Lighthouse	5.7952° South	35.1853° West	50	Brazil	Instituto de Pesquisas Energeticas e Nucleares, II Centro de Quimica e Meio Ambiente, Divisao de Quimica Ambiental
NMB		Gobabeb	23.58° South	15.03° East	456	Namibia	Gobabeb Training and Research Center
NWR 		Niwot Ridge, Colorado	40.0531° North	105.5864° West	3523	United States	University of Colorado/INSTAAR
OKX 		Ochsenkopf	50.0301° North	11.8084° East	1022	Germany	Max Planck Institute for Biogeochemistry
PAL 		Pallas-Sammaltunturi, GAW Station	67.9733° North	24.1157° East	565	Finland	Finnish Meteorological Institute
PSA 		Palmer Station, Antarctica	64.7742° South	64.0527° West	10	United States	National Science Foundation
RPB 		Ragged Point	13.165° North	59.432° West	15	Barbados	Private Party
SDZ		Shangdianzi	40.65° North	117.117° East	293	China	Chinese Academy of Meteorological Sciences (CAMS) and Beijing Meteorological Bureau (BMB), China Meteorological Administration (CMA)
SEY 		Mahe Island	4.6824° South	55.5325° East	2	Seychelles	Seychelles Bureau of Standards
SGP		Southern Great Plains, Oklahoma	36.607° North	97.489° West	314	United States	Lawrence Berkeley National Laboratory
SHM 		Shemya Island, Alaska	52.7112° North	174.126° East	23	United States	Chugach McKinley
SMO 		Tutuila	14.2474° South	170.5644° West	42	American Samoa	NOAA Global Monitoring Laboratory
SPO 		South Pole, Antarctica	89.98° South	24.8° West	2810	United States	National Science Foundation
SUM 		Summit	72.5962° North	38.422° West	3209.54	Greenland	National Science Foundation
SYO 		Syowa Station, Antarctica	69.0125° South	39.59° East	14	Japan	Office of Polar Programs
TAP 		Tae-ahn Peninsula	36.7376° North	126.1328° East	16	Republic of Korea	National Institute of Polar Research
THD 		Trinidad Head, California	41.0541° North	124.151° West	107	United States	Korea Centre for Atmospheric Environment Research
TIK 		Hydrometeorological Observatory of Tiksi	71.5965° North	128.8887° East	19	Russia	Scientific Aviation, Inc., NOAA Global Monitoring Laboratory, AGAGE, Scripps Institution of Oceanography, Humboldt State University Marine Laboratory
TPI 		Taiping Island	10.3786° North	114.3711° East	4	Taiwan	
USH		Ushuaia	54.8484° South	68.3106° West	12	Argentina	Servicio Meteorologico Nacional
UTA		Wendover, Utah	39.9018° North	113.7181° West	1327	United States	Beth Anderson/NWS Cooperative Observer
UUM		Ulaan Uul	44.4516° North	111.0956° East	1007	Mongolia	Mongolian Hydrometeorological Research Institute
WIS		Weizmann Institute of Science at the Arava Institute, Kurnia	29.9646° North	35.0605° East	151	Israel	Weizmann Institute of Science and Arava Institute for Environmental Studies
WLG		Mt. Waliguan	36.2879° North	100.8964° East	20 3810	Peoples Republic of China	Chinese Academy of Meteorological Sciences (CAMS) and Qinghai Meteorological Bureau (QMB), China Meteorological Administration (CMA)
ZEP		Ny-Alesund, Svalbard	78.9067° North	11.8883° East	474	Norway and Sweden	Zeppelin Station/University of Stockholm Meteorological Institute

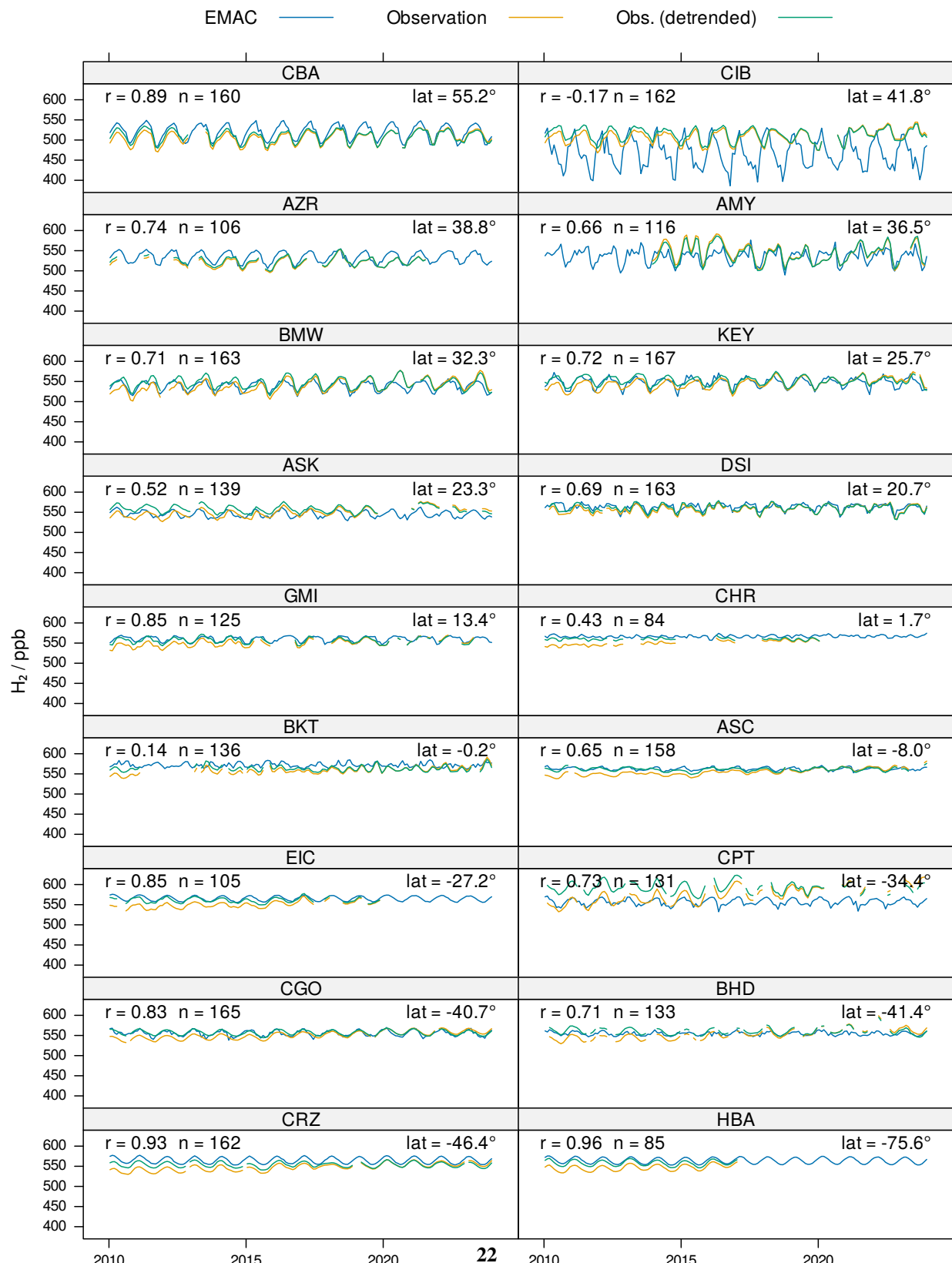


Figure B1. Time series comparison of observational and EMAC model data for H_2 . Latitudes are denoted by lat. [Other stations part 1]

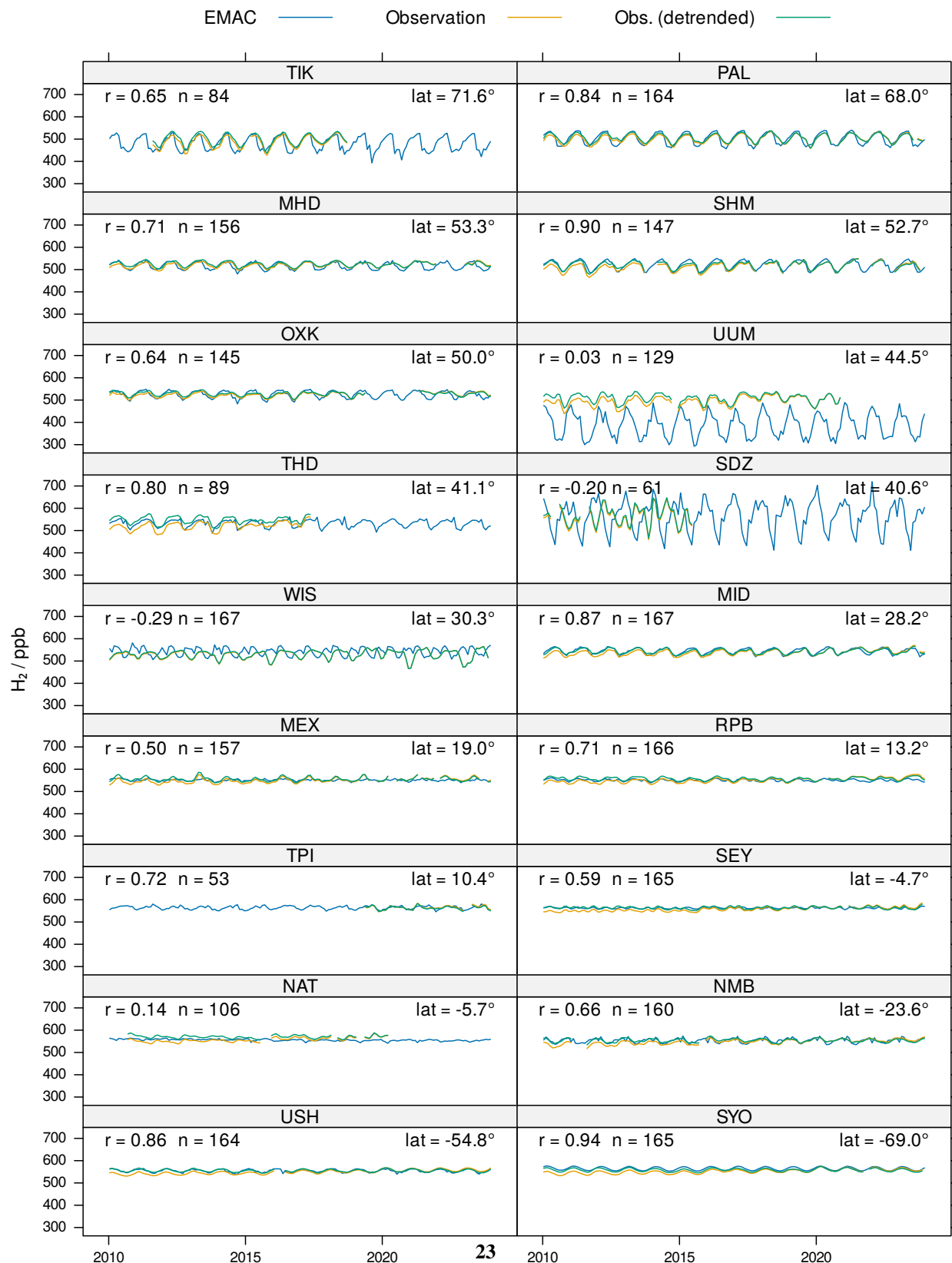


Figure B2. Time series comparison of observational and EMAC model data for H_2 . Latitudes are denoted by lat. [Other stations part 2]

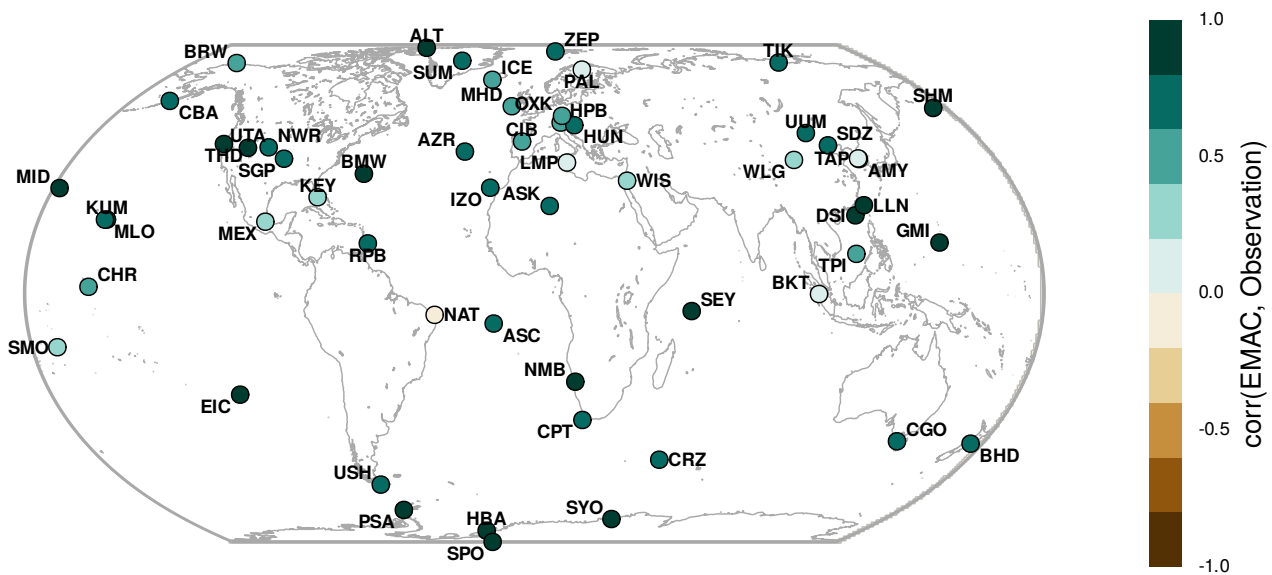


Figure B3. Pearson correlation coefficient between EMAC CH₄ mixing ratios and observational data. Model data is compared with detrended observational data for the years 2010–2023 (inclusive) to perform [this](#)[these](#) calculations. For a more extensive comparison see Zimmermann et al. (2020).

Table B1. Comparison of mean model and observational H₂ mixing ratios. Δ = Model – Observed, while r denotes the Pearson correlation coefficient. In the case of the BKT station, the EMAC value of one grid cell to the west of the station is used as it is considered more representative.

heightStation	Longitude	Latitude	# values	H ₂ EMAC (ppb)	H ₂ Observed (ppb)	Δ (ppb)	r
ALT <u>pma</u>	-62.5	82.5	168	504.	501.	3.19	0.93
ZEP <u>pnam</u>	11.9	78.9	168	515.	513.	1.87	0.94
SUM <u>pn</u>	-38.4	72.6	168	522.	526.	-4.00	0.81
TIK <u>pma</u>	129.	71.6	84	479.	499.	-19.8	0.65
BRW <u>pma</u>	-157.	71.3	168	502.	507.	-4.82	0.81
PAL <u>pn</u>	24.1	68.0	164	503.	506.	-3.01	0.84
ICE <u>pma</u>	-20.3	63.4	168	518.	522.	-3.95	0.86
CBA <u>ma</u>	-163.	55.2	160	520.	510.	9.96	0.89
MHD <u>ma</u>	-9.90	53.3	156	517.	525.	-8.03	0.71
SHM <u>ma</u>	174.	52.7	147	521.	518.	2.89	0.90
OXK <u>m</u>	11.8	50.0	145	525.	528.	-3.19	0.64
HPB <u>m</u>	11.0	47.8	168	526.	527.	-1.10	0.56
HUN	16.7	47.0	168	513.	523.	-9.78	0.39
UUM	111.	44.5	129	388.	508.	-121.	0.034
CIB	-4.93	41.8	162	467.	514.	-46.9	-0.17
THD <u>ma</u>	-124.	41.1	89	532.	547.	-15.0	0.80
SDZ	117.	40.6	61	566.	569.	-2.98	-0.20
NWR <u>m</u>	-106.	40.1	168	547.	536.	11.2	0.59
UTA	-114.	39.9	168	527.	514.	12.8	0.82
AZR <u>ma</u>	-27.4	38.8	106	533.	523.	10.4	0.74
TAP <u>ma</u>	126.	36.7	168	535.	547.	-12.7	0.62
SGP	-97.5	36.6	168	507.	519.	-12.2	0.77
AMY <u>ma</u>	126.	36.5	116	536.	543.	-7.17	0.66
WLG <u>m</u>	101.	36.3	168	527.	529.	-1.29	0.56
LMP <u>ma</u>	12.6	35.5	168	517.	532.	-14.5	0.046
BMW <u>ma</u>	-64.9	32.3	163	539.	546.	-7.09	0.71
WIS	35.0	30.3	167	544.	530.	13.8	-0.29
IZO <u>mma</u>	-16.5	28.3	168	545.	551.	-6.18	0.61
MID <u>ma</u>	-177.	28.2	167	544.	543.	0.830	0.87
KEY <u>ma</u>	-80.2	25.7	167	548.	552.	-3.73	0.72
LLN <u>m</u>	121.	23.5	168	563.	565.	-1.83	0.63
ASK <u>m</u>	5.63	23.3	139	545.	558.	-13.1	0.52
DSI <u>ma</u>	117.	20.7	163	563.	560.	2.75	0.69
KUM <u>ma</u>	-155.	19.6	168	544.	544.	0.133	0.75
MILO <u>mma</u>	-156.	19.5	168	558.	548.	10.4	0.70
MEX <u>m</u>	-97.3	19.0	157	551.	556.	-5.06	0.50
GMI <u>ma</u>	145.	13.4	125	560.	557.	3.36	0.85
RPB <u>ma</u>	-59.4	13.2	166	550.	557.	-6.91	0.71
TPI <u>ma</u>	114.	10.4	53	565.	563.	1.58	0.72
CHR <u>ma</u>	-157.	1.70	84	567.	560.	7.12	0.43
BKT <u>mma</u>	100.	-0.202	136	572.	563.	8.29	0.14
SEY <u>ma</u>	55.5	-4.68	165	563.	564.	-1.10	0.59
NAT <u>ma</u>	-35.2	-5.68	106	554.	570.	-16.9	0.14
ASC <u>ma</u>	-14.4	-7.97	158	562.	561.	1.26	0.65
SMO <u>ma</u>	-171.	-14.2	168	567.	561.	5.54	0.65
NMB	15.0	-23.6	160	554.	554.	0.158	0.66
EIC <u>ma</u>	-109.	-27.2	105	565.	561.	4.23	0.85
CPT <u>ma</u>	18.5	-34.4	131	557.	593.	-35.8	0.73
CGO <u>ma</u>	145.	-40.7	165	555.	557.	-1.56	0.83
BHD <u>ma</u>	175.	-41.4	133	554.	561.	-6.38	0.71
CRZ <u>ma</u>	51.8	-46.4	162	564.	554.	10.3	0.93
USH <u>ma</u>	-68.3	-54.8	164	554.	556.	-1.20	0.86
PSA <u>pma</u>	-64.1	-64.8	168	564.	557.	6.43	0.95
SYO <u>pma</u>	39.6	-69.0	165	564.	558.	6.05	0.94
HBA <u>pma</u>	-26.2	-75.6	85	564.	558.	5.79	0.96
SPO <u>pm</u>	-24.8	-89.5	168	564.	558.	5.81	0.96

Author contributions. JL managed the project with contributions from AP. BS led the delivery of model simulations with contributions from AP, KK, SG, CB and NS. KK led the delivery of soil sink modelling with contributions from BS. CB led the collation of observational data and its quality control with contributions from BS. SG led the delivery of chemical tagging with contributions from BS. NS wrote the manuscript with contributions from all co-authors. All authors met to discuss the results and contributed to the writing and editing of the 375 manuscript.

Competing interests. We declare that two of the co-authors hold an editorial board position with Geoscientific Model Development. The authors have no other competing interests to declare.

Acknowledgements

N. S. acknowledges funding support from the CSIRO International Hydrogen Research Fellowship scheme and the Faculty of 380 Engineering and Information Technology at UTS to undertake a sabbatical at the Max Planck Institute for Chemistry in Mainz. All simulations were performed with the Levante High Performance Computing System (<https://www.dkrz.de/en/systems/hpc/hlre-4-levante>) hosted by Deutsches Klimarechenzentrum GmbH.

References

Akagi, S. K., Yokelson, R. J., Wiedinmyer, C., Alvarado, M. J., Reid, J. S., Karl, T., Crounse, J. D., and Wennberg, P. O.: Emission factors for open and domestic biomass burning for use in atmospheric models, *Atmospheric Chemistry and Physics*, 11, 4039–4072, 385 <https://doi.org/10.5194/acp-11-4039-2011>, 2011.

Andreae, M. O.: Emission of trace gases and aerosols from biomass burning—an updated assessment, *Atmospheric Chemistry and Physics*, 19, 8523–8546, 390 <https://doi.org/10.5194/acp-19-8523-2019>, 2019.

Archibald, A. T., Levine, J. G., Abraham, N. L., Cooke, M. C., Edwards, P. M., Heard, D. E., Jenkin, M. E., Karunaharan, A., Pike, R. C., Monks, P. S., Shallcross, D. E., Telford, P. J., Whalley, L. K., and Pyle, J. A.: Impacts of HO_x regeneration and recycling in the oxidation of isoprene: Consequences for the composition of past, present and future atmospheres, *Geophysical Research Letters*, 38, L05 804, 395 <https://doi.org/10.1029/2010gl046520>, 2011.

Bourtsoukidis, E., Pozzer, A., Sattler, T., Matthaios, V. N., Ernle, L., Edtbauer, A., Fischer, H., Könemann, T., Osipov, S., Paris, J.-D., Pfannerstill, E. Y., Stönnér, C., Tadic, I., Walter, D., Wang, N., Lelieveld, J., and Williams, J.: The Red Sea Deep Water is a potent source 395 of atmospheric ethane and propane, *Nature Communications*, 11, 447, <https://doi.org/10.1038/s41467-020-14375-0>, 2020.

Brasseur, G. P., Kiehl, J. T., Müller, J.-F., Schneider, T., Granier, C., Tie, X. X., and Hauglustaine, D.: Past and future changes in global tropospheric ozone: Impact on radiative forcing, *Geophysical Research Letters*, 25, 3807–3810, 400 <https://doi.org/10.1029/1998gl900013>, 1998.

Brenninkmeijer, C. A. M., Crutzen, P., Boumard, F., Dauer, T., Dix, B., Ebinghaus, R., Filippi, D., Fischer, H., Franke, H., Frieß, U., Heintzenberg, J., Helleis, F., Hermann, M., Kock, H. H., Koeppel, C., Lelieveld, J., Leuenberger, M., Martinsson, B. G., Miemczyk, S., 405 Moret, H. P., Nguyen, H. N., Nyfeler, P., Oram, D., O’Sullivan, D., Penkett, S., Platt, U., Pupek, M., Ramonet, M., Randa, B., Reichelt, M., Rhee, T. S., Rohwer, J., Rosenfeld, K., Scharffe, D., Schlager, H., Schumann, U., Slemr, F., Sprung, D., Stock, P., Thaler, R., Valentino, F., van Velthoven, P., Waibel, A., Wandel, A., Waschitschek, K., Wiedensohler, A., Xueref-Remy, I., Zahn, A., Zech, U., and Ziereis, H.: Civil Aircraft for the regular investigation of the atmosphere based on an instrumented container: The new CARIBIC system, *Atmospheric 410 Chemistry and Physics*, 7, 4953–4976, <https://doi.org/10.5194/acp-7-4953-2007>, 2007.

Collins, W. J., Lamarque, J.-F., Schulz, M., Boucher, O., Eyring, V., Hegglin, M. I., Maycock, A., Myhre, G., Prather, M., Shindell, D., and Smith, S. J.: AerChemMIP: quantifying the effects of chemistry and aerosols in CMIP6, *Geoscientific Model Development*, 10, 585–607, 415 <https://doi.org/10.5194/gmd-10-585-2017>, 2017.

Derwent, R., Simmonds, P., O’Doherty, S., Manning, A., Collins, W., and Stevenson, D.: Global environmental impacts of the hydrogen economy, *International Journal of Nuclear Hydrogen Production and Application*, 1, 57–67, <https://doi.org/10.1504/IJNHPA.2006.009869>, 2006.

Derwent, R. G., Stevenson, D. S., Utembe, S. R., Jenkin, M. E., Khan, A. H., and Shallcross, D. E.: Global modelling studies of hydrogen and its isotopomers using STOCHEM-CRI: Likely radiative forcing consequences of a future hydrogen economy, *International Journal of Hydrogen Energy*, 45, 9211–9221, <https://doi.org/10.1016/j.ijhydene.2020.01.125>, 2020.

Ehhalt, D. H. and Rohrer, F.: The tropospheric cycle of H₂: a critical review, *Tellus B: Chemical and Physical Meteorology*, 61B, 500—535, 415 <https://doi.org/10.1111/j.1600-0889.2009.00416.x>, 2009.

Ehhalt, D. H. and Rohrer, F.: The dependence of soil H₂ uptake on temperature and moisture: a reanalysis of laboratory data, *Tellus B: Chemical and Physical Meteorology*, 63B, 1040—1051, <https://doi.org/10.1111/j.1600-0889.2011.00581.x>, 2011.

Ehhalt, D. H. and Rohrer, F.: Deposition velocity of H₂: a new algorithm for its dependence on soil moisture and temperature, *Tellus B: Chemical and Physical Meteorology*, 65, 19 904, <https://doi.org/10.3402/tellusb.v65i0.19904>, 2013a.

Ehhalt, D. H. and Rohrer, F.: Dry deposition of molecular hydrogen in the presence of H₂ production, *Tellus B: Chemical and Physical Meteorology*, 65, 20 620, <https://doi.org/10.3402/tellusb.v65i0.20620>, 2013b.

Ellis, G. S. and Gelman, S. E.: Model predictions of global geologic hydrogen resources, *Science Advances*, 10, eado0955, <https://doi.org/10.1126/sciadv.ado0955>, 2024.

425 Esquivel-Elizondo, S., Hormaza Mejia, A., Sun, T., Shrestha, E., Hamburg, S. P., and Ocko, I. B.: Wide range in estimates of hydrogen emissions from infrastructure, *Frontiers in Energy Research*, 11, 1207 208, <https://doi.org/10.3389/fenrg.2023.1207208>, 2023.

Fan, Z., Sheerazi, H., Bhardwaj, A., Corbeau, A.-S., Longobardi, K., Castañeda, A., Merz, A.-K., Woodall, C. M., Agrawal, M., Orozco-Sanchez, S., and Friedmann, J.: Hydrogen leakage: a potential risk for the hydrogen economy, The Center on Global Energy Policy at Columbia University, pp. 1-33, https://www.energypolicy.columbia.edu/sites/default/files/file-uploads/HydrogenLeakageRegulations_CGEP_Commentary_063022.pdf (last access: 6 Septemer 2024), 2022.

430 Galimova, T., Ram, M., and Breyer, C.: Mitigation of air pollution and corresponding impacts during a global energy transition towards 100% renewable energy system by 2050, *Energy Reports*, 8, 14 124–14 143, <https://doi.org/10.1016/j.egyr.2022.10.343>, 2022.

Ganzeveld, L., Bouwman, L., Stehfest, E., van Vuuren, D. P., Eickhout, B., and Lelieveld, J.: Impact of future land use and land cover changes on atmospheric chemistry-climate interactions, *Journal of Geophysical Research: Atmospheres*, 115, D23 301, <https://doi.org/10.1029/2010jd014041>, 2010.

435 Giglio, L., Randerson, J. T., and van der Werf, G. R.: Analysis of daily, monthly, and annual burned area using the fourth-generation global fire emissions database (GFED4), *Journal of Geophysical Research: Biogeosciences*, 118, 317–328, <https://doi.org/10.1002/jgrg.20042>, 2013.

GLDAS: GLDAS Soil Land Surface, <https://ldas.gsfc.nasa.gov/gldas/soils>, (last access: 24 September 2024), 2024.

440 Granier, C., Darras, S., Denier van der Gon, H., Doubalova, J., Elguindi, N., Galle, B., Gauss, M., Guevara, M., Jalkanen, J.-P., Kuenen, J., Liouesse, C., Quack, B., Simpson, D., and Sindelarova, K.: The Copernicus Atmosphere Monitoring Service global and regional emissions (April 2019 version), Copernicus Atmosphere Monitoring Service (CAMS) report, pp. 1–54, <https://doi.org/10.24380/d0bn-kx16>, 2019.

Guenther, A., Hewitt, C. N., Erickson, D., Fall, R., Geron, C., Graedel, T., Harley, P., Klinger, L., Lerdau, M., McKay, W. A., Pierce, T., Scholes, B., Steinbrecher, R., Tallamraju, R., Taylor, J., and Zimmerman, P.: A global model of natural volatile organic compound emissions, *Journal of Geophysical Research: Atmospheres*, 100, 8873–8892, <https://doi.org/10.1029/94JD02950>, 1995.

445 Hand, E.: Hidden Hydrogen. Does Earth hold vast stores of a renewable carbon-free fuel?, *Science*, 379, 630–636, <https://doi.org/10.1126/science.adh1460>, 2023.

Hauglustaine, D. A. and Ehhalt, D. H.: A three-dimensional model of molecular hydrogen in the troposphere, *Journal of Geophysical Research: Atmospheres*, 107, 4330, <https://doi.org/10.1029/2001JD001156>, 2002.

450 Hersbach, H., Bell, B., Berrisford, P., Hirahara, S., Horányi, A., Muñoz-Sabater, J., Nicolas, J., Peubey, C., Radu, R., Schepers, D., Simmons, A., Soci, C., Abdalla, S., Abellán, X., Balsamo, G., Bechtold, P., Biavati, G., Bidlot, J., Bonavita, M., De Chiara, G., Dahlgren, P., Dee, D., Diamantakis, M., Dragani, R., Flemming, J., Forbes, R., Fuentes, M., Geer, A., Haimberger, L., Healy, S., Hogan, R. J., Hólm, E., Janisková, M., Keeley, S., Laloyaux, P., Lopez, P., Lupu, C., Radnoti, G., de Rosnay, P., Rozum, I., Vamborg, F., Vil- laume, S., and Thépaut, J.-N.: The ERA5 global reanalysis, *Quarterly Journal of the Royal Meteorological Society*, 146, 1999–2049, <https://doi.org/10.1002/qj.3803>, 2020.

Hersbach, H., Bell, B., Berrisford, P., Biavati, G., Horányi, A., Muñoz Sabater, J., Nicolas, J., Peubey, C., Radu, R., Rozum, I., Schepers, D., Simmons, A., Soci, C., Dee, D., and Thépaut, J.-N.: ERA5 hourly data on single levels from 1940 to present, Copernicus Climate Change Service (C3S) Climate Data Store (CDS) (last access: 19 September 2024), <https://doi.org/10.24381/cds.adbb2d47>, 2023.

Houweling, S., Kaminski, T., Dentener, F., Lelieveld, J., and Heimann, M.: Inverse modeling of methane sources and sinks using the adjoint of a global transport model, *Journal of Geophysical Research: Atmospheres*, 104, 26 137–26 160, <https://doi.org/10.1029/1999JD900428>, 1999.

Hydrogen Council: Hydrogen for Net-Zero. A critical cost-competitive energy vector, pp. 1-56, <https://hydrogencouncil.com/en/hydrogen-for-net-zero/> (last access: 6 September 2024), 2021.

International Energy Agency: Energy Technology Perspectives 2020. Special Report on Carbon Capture Utilisation and Storage: CCUS in clean energy transitions., pp. 1-174, https://www.oecd-ilibrary.org/energy/energy-technology-perspectives-2020-special-report-on-carbon-capture-utilisation-and-storage_208b66f4-en (last access: 6 September 2024), 2020.

International Energy Agency: Global Hydrogen Review 2023, pp. 1-176, <https://www.iea.org/reports/global-hydrogen-review-2023> (last access: 6 September 2024), 2023.

Jöckel, P., Tost, H., Pozzer, A., Brühl, C., Buchholz, J., Ganzeveld, L., Hoor, P., Kerkweg, A., Lawrence, M. G., Sander, R., Steil, B., Stiller, G., Tanarhte, M., Taraborrelli, D., van Aardenne, J., and Lelieveld, J.: The atmospheric chemistry general circulation model ECHAM5/MESSy1: consistent simulation of ozone from the surface to the mesosphere, *Atmospheric Chemistry and Physics*, 6, 5067–5104, <https://doi.org/10.5194/acp-6-5067-2006>, 2006.

Jöckel, P., Kerkweg, A., Pozzer, A., Sander, R., Tost, H., Riede, H., Baumgaertner, A., Gromov, S., and Kern, B.: Development cycle 2 of the Modular Earth Submodel System (MESSy2), *Geoscientific Model Development*, 3, 717–752, <https://doi.org/10.5194/gmd-3-717-2010>, 2010.

Kaiser, J. W., Heil, A., Andreae, M. O., Benedetti, A., Chubarova, N., Jones, L., Morcrette, J.-J., Razinger, M., Schultz, M. G., Suttie, M., and van der Werf, G. R.: Biomass burning emissions estimated with a global fire assimilation system based on observed fire radiative power, *Biogeosciences*, 9, 527–554, <https://doi.org/10.5194/bg-9-527-2012>, 2012.

Kerkweg, A., Sander, R., Tost, H., and Jöckel, P.: Technical note: Implementation of prescribed (OFFLEM), calculated (ONLEM), and pseudo-emissions (TNUUDGE) of chemical species in the Modular Earth Submodel System (MESSy), *Atmospheric Chemistry and Physics*, 6, 3603–3609, <https://doi.org/10.5194/acp-6-3603-2006>, 2006.

Klingmüller, K.: Hydrogen deposition velocity, <https://doi.org/10.17617/3.PLYVTZ>, 2025.

Lan, X., Thoning, K., and Dlugokencky, E.: Trends in globally-averaged CH₄, N₂O, and SF₆ determined from NOAA Global Monitoring Laboratory measurements, <https://doi.org/10.15138/P8XG-AA10>, 2024.

Lelieveld, J., Berresheim, H., Borrmann, S., Crutzen, P. J., Dentener, F. J., Fischer, H., Feichter, J., Flatau, P. J., Heland, J., Holzinger, R., Kormann, R., Lawrence, M. G., Levin, Z., Markowicz, K. M., Mihalopoulos, N., Minikin, A., Ramanathan, V., de Reus, M., Roelofs, G. J., Scheeren, H. A., Sciare, J., Schlager, H., Schultz, M., Siegmund, P., Steil, B., Stephanou, E. G., Stier, P., Traub, M., Warneke, C., Williams, J., and Ziereis, H.: Global Air Pollution Crossroads over the Mediterranean, *Science*, 298, 794–799, <https://doi.org/10.1126/science.1075457>, 2002.

Lelieveld, J., Gromov, S., Pozzer, A., and Taraborrelli, D.: Global tropospheric hydroxyl distribution, budget and reactivity, *Atmospheric Chemistry and Physics*, 16, 12 477–12 493, <https://doi.org/10.5194/acp-16-12477-2016>, 2016.

Martin, A., Gayler, V., Steil, B., Klingmüller, K., Jöckel, P., Tost, H., Lelieveld, J., and Pozzer, A.: Evaluation of the coupling of EMACv2.55 to the land surface and vegetation model JSBACHv4, *Geoscientific Model Development*, 17, 5705–5732, <https://doi.org/10.5194/gmd-17-5705-2024>, 2024.

495 Millington, R. J. and Quirk, J. P.: Permeability of Porous Media, *Nature*, 183, 387–388, <https://doi.org/10.1038/183387a0>, 1959.

Nicely, J. M., Duncan, B. N., Hanisco, T. F., Wolfe, G. M., Salawitch, R. J., Deushi, M., Haslerud, A. S., Jöckel, P., Josse, B., Kinnison, D. E., Klekociuk, A., Manyin, M. E., Marécal, V., Morgenstern, O., Murray, L. T., Myhre, G., Oman, L. D., Pitari, G., Pozzer, A., Quaglia, I., Revell, L. E., Rozanov, E., Stenke, A., Stone, K., Strahan, S., Tilmes, S., Tost, H., Westervelt, D. M., and Zeng, G.: A machine learning examination of hydroxyl radical differences among model simulations for CCM1-1, *Atmospheric Chemistry and Physics*, 20, 1341–1361, 500 <https://doi.org/10.5194/acp-20-1341-2020>, 2020.

Novelli, P. C., Lang, P. M., Masarie, K. A., Hurst, D. F., Myers, R., and Elkins, J. W.: Molecular hydrogen in the troposphere: Global distribution and budget, *Journal of Geophysical Research: Atmospheres*, 104, 30 427–30 444, <https://doi.org/10.1029/1999JD900788>, 1999.

Ocko, I. B. and Hamburg, S. P.: Climate consequences of hydrogen emissions, *Atmospheric Chemistry and Physics*, 22, 9349–9368, 505 <https://doi.org/10.5194/acp-22-9349-2022>, 2022.

Paulot, F., Paynter, D., Naik, V., Malyshev, S., Menzel, R., and Horowitz, L. W.: Global modeling of hydrogen using GFDL-AM4.1: Sensitivity of soil removal and radiative forcing, *International Journal of Hydrogen Energy*, 46, 13 446–13 460, <https://doi.org/10.1016/j.ijhydene.2021.01.088>, 2021.

510 Paulot, F., Pétron, G., Crotwell, A. M., and Bertagni, M. B.: Reanalysis of NOAA H₂ observations: implications for the H₂ budget, *Atmospheric Chemistry and Physics*, 24, 4217–4229, <https://doi.org/10.5194/acp-24-4217-2024>, 2024.

Pétron, G., Crotwell, A. M., Madronich, M., Moglia, E., Baugh, K. E., Kitzis, D., Mefford, T., DeVogel, S., Neff, D., Lan, X., Crotwell, M. J., Thoning, K., Wolter, S., and Mund, J. W.: Atmospheric Hydrogen Dry Air Mole Fractions from the NOAA GML Carbon Cycle Cooperative Global Air Sampling Network, 2009–2023 Version: 2024-07-30, <https://doi.org/10.15138/WP0W-EZ08>, 2024.

Pieterse, G., Krol, M. C., Batenburg, A. M., Steele, L. P., Krumbel, P. B., Langenfelds, R. L., and Röckmann, T.: Global modelling of H₂ mixing ratios and isotopic compositions with the TM5 model, *Atmospheric Chemistry and Physics*, 11, 7001–7026, 515 <https://doi.org/10.5194/acp-11-7001-2011>, 2011.

Plummer, D., Nagashima, T., Tilmes, S., Archibald, A., Chiodo, G., Fadnavis, S., Gurney, H., Josse, B., Kim, J., Lamarque, J.-F., Morgenstern, O., Murray, L., Orbe, C., Tai, A., Chipperfield, M., Funke, B., Juckes, M., Kinnison, D., Kunze, M., Luo, B., Matthes, K., Newman, P. A., Pascoe, C., and Peter, T.: CCM1-2022: a new set of Chemistry–Climate Model Initiative (CCMI) community simulations to update 520 the assessment of models and support upcoming ozone assessment activities, *SPARC Newsletter*, https://www.aparc-climate.org/wp-content/uploads/2021/07/SPARCnewsletter_Jul2021_web.pdf (last access: 13 September 2025), 57, 22–30, 2021.

Pöschl, U., von Kuhlmann, R., Poisson, N., and Crutzen, P. J.: Development and intercomparison of condensed isoprene oxidation mechanisms for global atmospheric modeling, *Journal of Atmospheric Chemistry*, 37, 29–52, <https://doi.org/10.1023/A:1006391009798>, 2000.

Prather, M. J. and Zhu, L.: Resetting tropospheric OH and CH₄ lifetime with ultraviolet H₂O absorption, *Science*, 385, 201–204, 525 <https://doi.org/10.1126/science.adn0415>, 2024.

Prather, M. J., Holmes, C. D., and Hsu, J.: Reactive greenhouse gas scenarios: Systematic exploration of uncertainties and the role of atmospheric chemistry, *Geophysical Research Letters*, 39, 1–5, <https://doi.org/10.1029/2012GL051440>, 2012.

Price, H., Jaeglé, L., Rice, A., Quay, P., Novelli, P. C., and Gammon, R.: Global budget of molecular hydrogen and its deuterium content: Constraints from ground station, cruise, and aircraft observations, *Journal of Geophysical Research: Atmospheres*, 112, D22 108, 530 <https://doi.org/10.1029/2006JD008152>, 2007.

Randerson, J. T., van der Werf, G. R., Giglio, L., Collatz, G. J., and Kasibhatla, P. S.: Global fire emissions database, version 4.1 (GFEDv4), ORNL DAAC, Oak Ridge, Tennessee, USA. https://daac.ornl.gov/cgi-bin/dsviewer.pl?ds_id=1293 (last access: 22 December 2024), <https://doi.org/10.3334/ORNLDaac/1293>, 2017.

Reifenberg, S. F., Martin, A., Kohl, M., Bacer, S., Hamryszczak, Z., Tadic, I., Röder, L., Crowley, D. J., Fischer, H., Kaiser, K., Schneider, J., 535 Dörich, R., Crowley, J. N., Tomsche, L., Marsing, A., Voigt, C., Zahn, A., Pöhlker, C., Holanda, B. A., Krüger, O., Pöschl, U., Pöhlker, M., Jöckel, P., Dorf, M., Schumann, U., Williams, J., Bohn, B., Curtius, J., Harder, H., Schlager, H., Lelieveld, J., and Pozzer, A.: Numerical simulation of the impact of COVID-19 lockdown on tropospheric composition and aerosol radiative forcing in Europe, *Atmospheric Chemistry and Physics*, 22, 10 901–10 917, <https://doi.org/10.5194/acp-22-10901-2022>, 2022.

Rhee, T. S., Brenninkmeijer, C. A. M., Braß, M., and Brühl, C.: Isotopic composition of H₂ from CH₄ oxidation in the stratosphere and the 540 troposphere, *Journal of Geophysical Research: Atmospheres*, 111, D23 303, <https://doi.org/10.1029/2005JD006760>, 2006.

Righi, M., Hendricks, J., and Sausen, R.: The global impact of the transport sectors on atmospheric aerosol: simulations for year 2000 545 emissions, *Atmospheric Chemistry and Physics*, 13, 9939–9970, <https://doi.org/10.5194/acp-13-9939-2013>, 2013.

Rodell, M., Houser, P. R., Jambor, U., Gottschalck, J., Mitchell, K., Meng, C.-J., Arsenault, K., Cosgrove, B., Radakovich, J., Bosilovich, M., 550 Entin, J. K., Walker, J. P., Lohmann, D., and Toll, D.: The Global Land Data Assimilation System, *Bulletin of the American Meteorological Society*, 85, 381–394, <https://doi.org/10.1175/BAMS-85-3-381>, 2004.

Roeckner, E., Bäuml, G., Bonaventura, L., Brokopf, R., Esch, M., Giorgi, M., Hagemann, S., Kirchner, I., Kornblueh, L., Manzini, E., Rhodin, A., Schlese, U., Schulzweida, U., and Tompkins, A.: Report No 349: the atmospheric general circulation model ECHAM5, Part I., pp. 1–133, https://pure.mpg.de/pubman/faces/ViewItemOverviewPage.jsp?itemId=item_995269 (last access: 22 December 2024), 2003.

Roeckner, E., Brokopf, R., Esch, M., Giorgi, M., Hagemann, S., Kornblueh, L., Manzini, E., Schlese, U., and Schulzweida, U.: 555 Report No. 354: the atmospheric general circulation model ECHAM5, Part II., pp. 1–64, https://pure.mpg.de/pubman/faces/ViewItemOverviewPage.jsp?itemId=item_995221 (last access: 22 December 2024), 2004.

Roeckner, E., Brokopf, R., Esch, M., Giorgi, M., Hagemann, S., Kornblueh, L., Manzini, E., Schlese, U., and Schulzweida, U.: Sensitivity of Simulated Climate to Horizontal and Vertical Resolution in the ECHAM5 Atmosphere Model, *Journal of Climate*, 19, 3771–3791, 560 <https://doi.org/10.1175/JCLI3824.1>, 2006.

Sand, M., Skeie, R. B., Sandstad, M., Krishnan, S., Myhre, G., Bryant, H., Derwent, R., Hauglustaine, D., Paulot, F., Prather, M., and Stevenson, D.: A multi-model assessment of the Global Warming Potential of hydrogen, *Communications Earth & Environment*, 4, 203, <https://doi.org/10.1038/s43247-023-00857-8>, 2023.

Sanderson, M. G., Collins, W. J., Derwent, R. G., and Johnson, C. E.: Simulation of Global Hydrogen Levels Using a Lagrangian Three-Dimensional Model, *Journal of Atmospheric Chemistry*, 46, 15–28, <https://doi.org/10.1023/A:1024824223232>, 2003.

Saunois, M., Martinez, A., Poulter, B., Zhang, Z., Raymond, P. A., Regnier, P., Canadell, J. G., Jackson, R. B., Patra, P. K., Bousquet, P., Ciais, P., Dlugokencky, E. J., Lan, X., Allen, G. H., Bastviken, D., Beerling, D. J., Belikov, D. A., Blake, D. R., Castaldi, S., Crippa, M., Deemer, B. R., Dennison, F., Etiöpe, G., Gedney, N., Höglund-Isaksson, L., Holgerson, M. A., Hopcroft, P. O., Hugelius, G., Ito, A., Jain, A. K., Janardanan, R., Johnson, M. S., Kleinen, T., Krummel, P. B., Lauerwald, R., Li, T., Liu, X., McDonald, K. C., Melton, J. R., Mühlé, J., Müller, J., Murguia-Flores, F., Niwa, Y., Noce, S., Pan, S., Parker, R. J., Peng, C., Ramonet, M., Riley, W. J., Rocher-Ros, G., 565 Rosentreter, J. A., Sasakawa, M., Segers, A., Smith, S. J., Stanley, E. H., Thanwerdas, J., Tian, H., Tsuruta, A., Tubiello, F. N., Weber,

T. S., van der Werf, G. R., Worthy, D. E. J., Xi, Y., Yoshida, Y., Zhang, W., Zheng, B., Zhu, Q., Zhu, Q., and Zhuang, Q.: Global Methane Budget 2000–2020, *Earth System Science Data*, 17, 1873–1958, <https://doi.org/10.5194/essd-17-1873-2025>, 2025.

Schultz, M. G., Diehl, T., Brasseur, G. P., and Zittel, W.: Air pollution and climate-forcing impacts of a global hydrogen economy, *Science*, 302, 624–627, <https://doi.org/10.1126/science.1089527>, 2003.

570 Schultz, M. G., Heil, A., Hoelzemann, J. J., Spessa, A., Thonicke, K., Goldammer, J. G., Held, A. C., Pereira, J. M., and van het Bolscher, M.: Global wildland fire emissions from 1960 to 2000, *Global Biogeochemical Cycles*, 22, GB2002, <https://doi.org/10.1029/2007GB003031>, 2008.

Seiler, W. and Conrad, R.: Dickinson, R. E. (editor). Contribution of tropical ecosystems to the global budgets of trace gases, especially CH₄, H₂, CO, and N₂O, in: *The Geophysiology of Amazonia: Vegetation and Climate Interactions*, pp. 133–162, John Wiley, New York, ISBN 575 0471845116, 1987.

Silver, B., Reddington, C. L., Chen, Y., and Arnold, S. R.: A decade of China's air quality monitoring data suggests health impacts are no longer declining, *Environment International*, 197, 109 318, <https://doi.org/https://doi.org/10.1016/j.envint.2025.109318>, 2025.

Smith-Downey, N. V., Randerson, J. T., and Eiler, J. M.: Temperature and moisture dependence of soil H₂ uptake measured in the laboratory, *Geophysical Research Letters*, 33, L14 813, <https://doi.org/10.1029/2006GL026749>, 2006.

580 SPARC: SPARC Report on the Lifetimes of Stratospheric Ozone-Depleting Substances, Their Replacements, and Related Species, Ko, M. and Newman, P. and Reimann, S. and Strahan, S. (editors), pp. 1-255, <https://www.aparc-climate.org/publications/sparc-reports/sparc-report-no-6/> (last access: 13 September 2025), 2013.

The MESSy Consortium: The Modular Earth Submodel System Version 2.55.2_no-branch_b4754874_H2, <https://doi.org/10.5281/zenodo.15211346>, 2025.

585 Tromp, T. K., Shia, R.-L., Allen, M., Eiler, J. M., and Yung, Y. L.: Potential environmental impact of a hydrogen economy on the stratosphere, *Science*, 300, 1740–1742, <https://doi.org/10.1126/science.1085169>, 2003.

Truche, L., Donzé, F.-V., Goskolli, E., Muceku, B., Loisy, C., Monnin, C., Dutoit, H., and Cerepi, A.: A deep reservoir for hydrogen drives intense degassing in the Bulqizë ophiolite, *Science*, 383, 618–621, <https://doi.org/10.1126/science.adk9099>, 2024.

590 Van Aardenne, J. A., Dentener, F. J., Olivier, J. G. J., Peters, J. A. H. W., and Ganzeveld, L. N.: The EDGAR 3.2 Fast track 2000 dataset (32FT2000), https://www.researchgate.net/profile/Frank-Dentener/publication/233894132_The_EDGAR_32_Fast_track_2000_dataset_32FT2000/links/02e7e52fa254d80ba000000/The-EDGAR-32-Fast-track-2000-dataset-32FT2000.pdf (last access: 22 December 2024), 32, 2005.

Warneck, P.: *Chemistry of the Natural Atmosphere.*, International Geophysics Series, Volume 41, pp. 1-757, Academic Press, San Diego, ISBN 9780080954684, 1988.

595 Warwick, N., Griffiths, P., Keeble, J., Archibald, A., Pyle, J., and Shine, K.: Atmospheric implications of increased Hydrogen use, University of Cambridge and University of Reading, pp. 1-75, <https://assets.publishing.service.gov.uk/media/624eca7fe90e0729f4400b99/atmospheric-implications-of-increased-hydrogen-use.pdf> (last access: 22 December 2024), 2022.

Warwick, N. J., Bekki, S., Nisbet, E. G., and Pyle, J. A.: Impact of a hydrogen economy on the stratosphere and troposphere studied in a 2-D model, *Geophysical Research Letters*, 31, L05 107, <https://doi.org/10.1029/2003GL019224>, 2004.

600 Warwick, N. J., Archibald, A. T., Griffiths, P. T., Keeble, J., O'Connor, F. M., Pyle, J. A., and Shine, K. P.: Atmospheric composition and climate impacts of a future hydrogen economy, *Atmospheric Chemistry and Physics*, 23, 13 451–13 467, <https://doi.org/10.5194/acp-23-13451-2023>, 2023.

Xiao, X., Prinn, R. G., Simmonds, P. G., Steele, L. P., Novelli, P. C., Huang, J., Langenfelds, R. L., O'Doherty, S., Krummel, P. B., Fraser, P. J., Porter, L. W., Weiss, R. F., Salameh, P., and Wang, R. H. J.: Optimal estimation of the soil uptake rate of molecular hydrogen from the Advanced Global Atmospheric Gases Experiment and other measurements, *Journal of Geophysical Research: Atmospheres*, 112, D07 303, <https://doi.org/10.1029/2006JD007241>, 2007.

Yang, L. H., Jacob, D. J., Lin, H., Dang, R., Bates, K. H., East, J. D., Travis, K. R., Pendergrass, D. C., and Murray, L. T.: Assessment of Hydrogen's Climate Impact Is Affected by Model OH Biases, *Geophysical Research Letters*, 52, e2024GL112445, <https://doi.org/10.1029/2024GL112445>, 2025.

Yashiro, H., Sudo, K., Yonemura, S., and Takigawa, M.: The impact of soil uptake on the global distribution of molecular hydrogen: chemical transport model simulation, *Atmospheric Chemistry and Physics*, 11, 6701–6719, <https://doi.org/10.5194/acp-11-6701-2011>, 2011.

Yokelson, R. J., Saharjo, B. H., Stockwell, C. E., Putra, E. I., Jayarathne, T., Akbar, A., Albar, I., Blake, D. R., Graham, L. L. B., Kurniawan, A., Meinardi, S., Ningrum, D., Nurhayati, A. D., Saad, A., Sakuntaladewi, N., Setianto, E., Simpson, I. J., Stone, E. A., Sutikno, S., Thomas, A., Ryan, K. C., and Cochrane, M. A.: Tropical peat fire emissions: 2019 field measurements in Sumatra and Borneo and synthesis with previous studies, *Atmospheric Chemistry and Physics*, 22, 10 173–10 194, <https://doi.org/10.5194/acp-22-10173-2022>, 2022.

Yonemura, S., Yokozawa, M., Kawashima, S., and Tsuruta, H.: Model analysis of the influence of gas diffusivity in soil on CO and H₂ uptake, *Tellus B: Chemical and Physical Meteorology*, 52B, 919–933, <https://doi.org/10.3402/tellusb.v52i3.17075>, 2000.

Zimmermann, P. H., Brenninkmeijer, C. A. M., Pozzer, A., Jöckel, P., Winterstein, F., Zahn, A., Houweling, S., and Lelieveld, J.: Model simulations of atmospheric methane (1997–2016) and their evaluation using NOAA and AGAGE surface and IAGOS-CARIBIC aircraft observations, *Atmospheric Chemistry and Physics*, 20, 5787–5809, <https://doi.org/10.5194/acp-20-5787-2020>, 2020.